JGR Solid Earth

RESEARCH ARTICLE
10.1029/2026JB033858

High Temperature Friction and Strength of Felsite and Basalt: Implications for Supercritical EGS at Krafla, Iceland

E. Rybacki[1], V. Schuster[1], J. Starke[2], and S. Incel[1]

[1]GFZ Helmholtz Centre for Geosciences, Potsdam, Germany, [2]Universität Potsdam, Potsdam, Germany

Key Points:

- The frictional and triaxial strength of felsite and basalt was studied in triaxial compression tests up to high temperatures (<1100°C)
- Partial melting and pore collapse cause decrease in bulk and frictional strength with increasing temperature for both rock types
- Creep-induced fracture closure of felsite is unlikely at fast strain rate, but not over the expected lifetime of a supercritical EGS

Correspondence to:

S. Incel,
sarah.incel@gfz.de

Citation:

Rybacki, E., Schuster, V., Starke, J., & Incel, S. (2026). High temperature friction and strength of felsite and basalt: Implications for supercritical EGS at Krafla, Iceland. *Journal of Geophysical Research: Solid Earth*, *131*, e2026JB033858. https://doi.org/10.1029/2026JB033858

Received 16 JAN 2026
Accepted 19 APR 2026

Author Contributions:

Conceptualization: E. Rybacki
Data curation: E. Rybacki, V. Schuster
Formal analysis: E. Rybacki, V. Schuster, J. Starke
Investigation: J. Starke
Methodology: E. Rybacki, V. Schuster, J. Starke, S. Incel
Supervision: E. Rybacki
Writing – original draft: E. Rybacki, V. Schuster
Writing – review & editing: V. Schuster, J. Starke, S. Incel

Abstract One promising potential site for extracting supercritical geothermal fluids is the Krafla volcano, Iceland, into which a borehole was drilled very close to a shallow rhyolite magma chamber at about 2 km depth. Besides the technical challenge to drill in this setting, the extreme temperature conditions of $T > 900$°C close to the magma body may significantly change the mechanical rock properties leading to low strength and fast closure of fracs, both of which are unfavorable for successfully operating a supercritical geothermal system (SCGS). Here, we determined experimentally the strength of dry felsite and basalt, lithologies that are important in the context of the Krafla Magma Testbed (KMT) project that aims to drill into or at least close to the magma chamber. The bulk triaxial strength of cylindrical samples and the frictional strength of split-cylinder samples with a preexisting shear plane were measured at about 50 MPa pressure and temperatures up to 1100°C using a Paterson gas-deformation apparatus. Peak compressive strength of the felsite starts to decrease strongly at $T \approx 900$°C and of basalt at about 700°C. The friction coefficient of felsite drops down at $T \approx 750$°C and of basalt at $T \approx 500$°C. Strength decrease at high temperature is associated with partial melting and/or pore collapse. The results indicate that fracture closure-related permeability reduction within the felsite contact aureole at high temperature due to passing the brittle plastic transition is unlikely at fast (laboratory) strain rate, but may occur at lower (in situ) strain rate.

Plain Language Summary Geothermal energy may substantially contribute to the increasing energy demand, in particular if fluids are extracted under supercritical conditions. The KMT project in Iceland is a promising test site to study such a geothermal system, where temperatures up to about 900°C were reached in a shallow borehole drilled close to a magma chamber. Such high temperatures may limit the efficiency of hot fluid extraction due to the collapse of connected pore and fracture networks by plastic creep processes. We studied the bulk and friction strength of felsite and basalt at in situ pressure and temperatures up to 1100°C, which are important rock types at depth in Krafla. The results show that the compressive strength of felsite decreases at temperatures higher than about 900°C and frictional strength drops down at temperatures higher than about 750°C. For basalt, the corresponding threshold temperatures are about 200°C lower. Because felsite is the predominant lithology adjacent to the magma chamber, we infer that pronounced deformation-induced permeability reduction is unlikely at fast strain rates. Extrapolation of existing plastic flow laws for the major constituents of these rocks to in situ conditions suggest that at low strain rates fracture network collapse is more likely.

1. Introduction

Within the context of the transition from using conventional carbon-containing energy resources toward a more sustainable and renewable energy supply, geothermal energy may play an important role in the future. Currently, geothermal energy accounts for less than 1% of the total energy consumption worldwide, but has the potential of a 10 times or higher contribution (Lavallée et al., 2020). In terms of profitable power generation, intermediate (125–225°C) and high temperature ($T > 225$°C) geothermal systems are of interest, which requires elevated heat flow and permeable structures in the underground (Jolie et al., 2021). Based on geoscientific and engineering criteria, Stimac et al. (2015) defined five different categories of geothermal resources, including young igneous systems with fracture networks formed above shallow magma intrusions, tectonic systems with fluid circulation along fault and fracture systems, deep sedimentary aquifers, hot dry rock systems, and supercritical and/or magma tap systems. A promising example of the latter type is the Krafla Magma Testbed project, located in Iceland.

Most promising and challenging are supercritical geothermal systems (SCGS), for which the efficiency may be 10 times higher than for systems operating below the critical point (Friðleifsson et al., 2014). The critical point of

pure water is at a temperature (T) of 374°C, at a pressure (P) of 22.1 MPa and seawater becomes critical at around $T = 406$°C and $P = 29.8$ MPa (Jolie et al., 2021; Reinsch et al., 2017). Currently existing supercritical geothermal systems are located or planned in Iceland (Krafla), Italy (Larderello), Japan (Kakkonda, Honshu), Kenya (Menengal), Mexico (Los Humeros), USA (The Geysers, Salton Sea, Newberry, Hawaii), and New Zealand (Taupo Volcanic Zone) (Asanuma et al., 2012; Jolie et al., 2021; Yapparova et al., 2023 and reference therein).

Typically, a reservoir permeability of more than about 1 mD (10^{-15} m^2) is desired to maintain sufficient productivity (Hayba & Ingebritsen, 1997; Jolie et al., 2021; Stimac et al., 2015). However, under supercritical conditions, corrosion, enhanced scaling (mineral precipitation) and reduced rock permeability may hinder economic energy production. In addition, the reservoir rock may not be able to maintain a sufficiently high porosity and fracture network for economic fluid circulation at such elevated temperatures, because plastic deformation processes may close the pores and cracks during the operation time of a SCGS or at least reduce their connectivity, so that the heat transport changes from advection to conduction-controlled. Therefore, reservoirs that are located at depth levels crossing the brittle plastic transition (BPT) are often considered to be inefficient (e.g., Stimac et al., 2015). Note that the BPT is often referred to as the brittle ductile transition (BDT), which is strictly speaking misleading. In geomechanics literature, the BDT usually refers to a change from macroscopically localized to non-localized deformation, whereas the BPT indicates the change in deformation mechanisms from brittle fracturing to plastic flow and usually requires higher temperatures to be activated than the BDT (e.g., Kohlstedt et al., 1995; Rutter, 1986; Rybacki et al., 2021). To enhance or maintain fluid flow, geothermal systems are often hydraulically stimulated that may sometimes induce seismicity, in particular if critically stressed pre-existing faults are reactivated (e.g., Olasolo et al., 2016; Zang et al., 2014). In this context, the frictional properties of rocks at in situ conditions are of interest since they determine fault stability and strength of a fractured reservoir. Accordingly, knowledge of mechanical properties of intact and fractured rocks at in situ conditions are required to assess the feasibility of a SCGS in terms of deformation mode and frictional strength. In-situ temperatures may be very high in some areas that are envisioned for some supercritical geothermal systems, for example, close to (or even within) a magma chamber (e.g., Elders et al., 2011; Árnason, 2020).

Here, we focus on the mechanical properties of felsite and basalt, rock types that are of interest for the KMT project, Iceland. The KMT project aims to better understand the behavior of magma and the surrounding hydrothermal system in the context of volcanic eruptions and release of geothermal energy (Eichelberger et al., 2018). It is located at the Krafla caldera volcano, N-E Iceland, which is a part of the Northern Volcanic Zone, representing the on-shore part of the Mid-Atlantic Ridge (e.g., Eggertsson et al., 2020). The project idea was born after a drilled borehole (IDDP-1) involuntarily hit a magma chamber with silicic (rhyolitic) melt at a depth of about 2.1 km in 2009 (e.g., Elders et al., 2011; Schuler et al., 2015). The well was designed to be drilled into supercritical fluids as a part of the Iceland deep drilling project and produced superheated steam at 14 MPa pressure and 450°C temperature at the wellhead for more than 2 years (Elders et al., 2014; Friðleifsson et al., , 2017). Evaluation of the cuttings obtained during drilling reveals that the stratigraphy of the rocks perforated by well IDDP-1 is dominated by intrusive igneous rocks (basaltic dykes, gabbro and felsite) at greater depth (>1,300 m) and extrusive rocks (lavas, ignimbrite, hyaloclastite) at shallow depth with various, depth dependent alteration zones (Eggertsson et al., 2020; Mortensen et al., 2014). The rhyolite melt possibly originated from partial melting of a hydrothermally altered basaltic crust at formation conditions of $P < 55$ MPa and $T = 850$–920°C (Zierenberg et al., 2013). Directly adjacent to the magma body is a felsite layer, forming an about 80 m thick crystallized magmatic aureole. Temperature within this layer is reduced by several hundred degrees Celsius over a few tens of meter thickness, where the hot inner part is assumed to deform in a plastic manner and is impermeable whereas the colder outer zone is brittle with microcracks that are connected to a hydrothermal system (Eichelberger et al., 2018).

So far, not much is known about the mechanical properties of felsite and basalt from Krafla at in situ conditions. Since no cores exist from IDDP-1, petrophysical data of felsite and basalt samples were measured on surface outcrop samples (Eggertsson, 2019; Eggertsson et al., 2020). Porosity of intact samples is 9%–18% for felsite and 11%–60% for basalt, respectively. Measured permeability is in the range of 10^{-15}–10^{-13} m^2 for felsite and 10^{-16}–10^{-13} m^2 for basalt, increasing with increasing porosity and after thermal pre-stressing (Eggertsson et al., 2020). Mechanical data of the two rock types were obtained at room temperature by Eggertsson (2019), revealing a high variability. In general, they show a trend of decreasing tensile strength (UTS), uniaxial

compressive strength (UCS), and Young's modulus (E) with increasing porosity. The triaxial strength increases with pressure, measured up to 30 MPa confining pressure (Eggertsson. 2019). In this study, we performed deformation experiments on intact and split-cylinder samples of felsite and basalt at confining pressures <90 MPa and temperatures up to 1100°C to determine the strength of intact as well as of pre-fractured (split-cylinder) rocks at simulated P-T conditions that are close to the expected conditions of the magma chamber at Krafla.

2. Experimental Methods

2.1. Starting Materials

Mechanical tests were done on two sets of samples: (a) felsite from Krafla (Iceland), collected from surface outcrops and kindly provided by Y. Lavallée (Ludwig Maximilian University of Munich) and (b) basalt from the extinct Rodderberg volcano south of Bonn, Germany (e.g., Paulick et al., 2009), kindly provided by N. Froitzheim (University of Bonn). The chemical composition of the two lithologies was determined by X-ray diffraction methods (XRD) and by using energy-dispersive spectroscopy (EDX) at the scanning-electron microscope (SEM, FEI Quanta 3D Dual Beam). Backscattered-electron (BSE) images, taken at the SEM, as well as images taken at the polarized light microscope were used to investigate the microstructures of the samples prior to and after the deformation tests.

The phaneritic, fine- to medium-grained (200 μm - 2 mm), holocrystalline felsite is mainly composed of plagioclase (≈43 wt%), quartz (≈35 wt%), alkali feldspar (≈13 wt%) and augite/pigeonite (total clinopyroxene≈8wt%) with few titanomagnetite/ilmenite (≈1 wt%) and accessory apatite (Figure 1). Prismatic euhedral plagioclase and subhedral clinopyroxenes of up to 2 mm in size display the largest mineral grains of the investigated felsite. The composition of plagioclase ranges from andesine to oligoclase (An_{10}–An_{45}), with larger mineral grains being more calciferous and occasionally exhibiting compositional zoning (Figure 1b). Euhedral, lath-shaped plagioclase crystals are frequently enveloped by intergrown anhedral quartz and alkali feldspar (Or_{20}–Or_{40}), forming a radiating granophyric texture, suggesting simultaneous crystallization of both phases close to the eutectic point. Similarly, augite and pigeonite are commonly intergrown and exhibit exsolution lamellae. The majority of clinopyroxene crystals co-exist with rounded, subhedral titanomagnetite/ilmenite (Figure 1c). Quartz is also present as anhedral grains, reaching sizes of up to 300 μm. The pore space consists of numerous inter- and transgranular microcracks (with apertures less than 20 μm) and frequent intergranular macropores with diameters of up to 3 mm, resulting in an average porosity of 10.0 ± 0.1 vol% (see Figure 1a and Table 1), as determined by helium pycnometry (using MIP Micromeritics AccuPyc 1330 & 1340). Estimated permeability derived from Hg-porosimetry (Porotec Pascal 144 & 440 Evo) is $\approx 10^{-13}$ m^2, which agrees well with the permeability reported by Eggertsson et al. (2020).

Based on total alkali–silica content (e.g., Le Maitre, 1984), basalt samples from Rodderberg can be classified as porphyritic to microcrystalline alkali basalt/basanite ($SiO_2 \approx 45$ wt%; $K_2O + Na_2O \approx 5$ wt%). Phenocrysts (≈5 vol%) primarily consist of olivine as well as small amounts of clinopyroxene (diopside) and plagioclase with crystals ranging between 1–5 mm in size (Figure 2). Olivine represents the largest phenocrysts, which are an- to subhedral, rich in MgO (≈Fo85) and exhibit undulatory extinction (Figure 2b) as well as light compositional zoning, with FeO enrichment toward the grain boundaries. Crystals are frequently fractured and exhibit alteration with precipitation of secondary iddingsite (Figure 2a). Quartz xenocrysts (<2 mm), which are surrounded by complex reaction rims, and also have secondary microcracks filled with secondary clay minerals, are rare (Figure 2c). The hyalopilitic groundmass is predominantly composed of fine-grained (≈10–400 μm) subhedral laths of plagioclase (total ≈32 wt%; An_{40}–An_{65}), subhedral laths and prisms of diopside (total ≈22 wt%), olivine (total ≈20 wt%; ≈Fo_{70}–Fo_{80}), titanomagnetite (<20 μm; total ≈5 wt%) and other accessory minerals (apatite, rutile). At the microscale, diopside and plagioclase crystals display a preferred orientation (Figure 2d). The remaining groundmass is composed of anhedral albite (≈13 wt%) and nepheline (≈13 wt%), which exhibit minor compositional variability and occur as interstitial phases between microliths. As a result, the groundmass is texturally heterogeneous and appears patchy in BSE images. Two distinct groundmass types can be distinguished: (a) an albite-rich variety characterized by a dense, low-porosity fabric, and (b) a nepheline-rich variety containing interparticle pores (<1%) with diameters of up to ~3 μm, which likely formed during magmatic flow and potentially degassing. Occasionally, microcracks occur within the groundmass, reaching lengths of up to

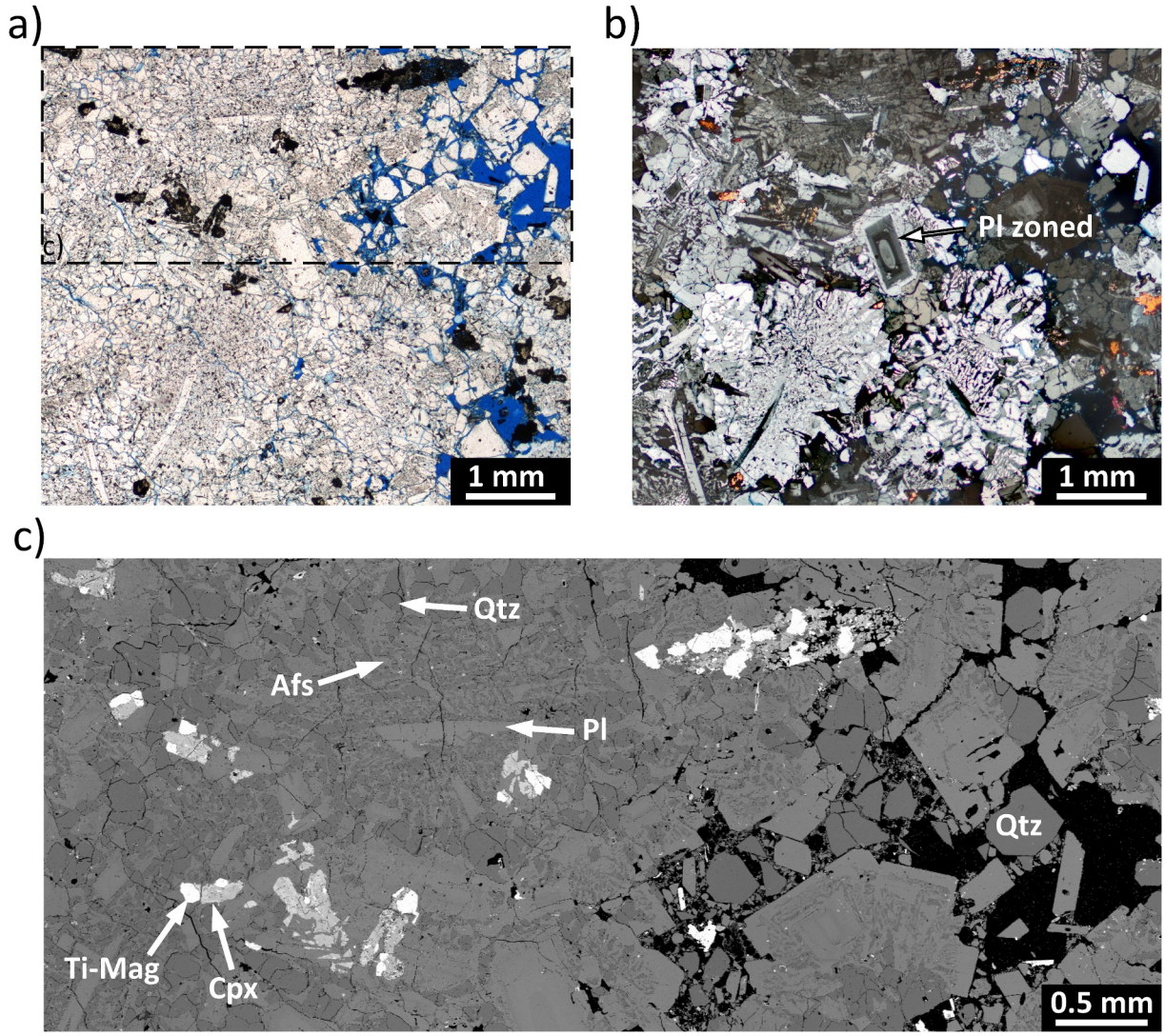

Figure 1. Microphotographs of undeformed felsite shown in plane- (a) and cross-polarized light (b). The area marked by the dashed line in (a) is magnified using backscattered electron (BSE) microscopy (c). Thin sections were impregnated with blue-colored epoxy, highlighting pores and microcracks (a). Larger plagioclase crystals show compositional zoning (Pl zoned) and are frequently surrounded by granophyric intergrowth of quartz and alkali feldspar (b). Clinopyroxene are composed of intergrown augite and pigeonite. Afs = alkali feldspar, Cpx = clinopyroxene, Pl = plagioclase, Ti-Mag = titanomagnetite, Qtz = quartz.

~250 μm and widths of about 5 μm. These cracks are consistently sealed by secondary clay minerals or by nepheline. Measured interconnected (He-) porosity is variable and ranges from 0.1 to 6.9 vol% (Tables 2 and 4).

In contrast to the tholeiitic basalts on Iceland, alkali basalts/basanites are critically silica undersaturated and contain feldspathoids. Based on drill cutting analysis and geophysical logs of well IDDP-1 at Krafla, Mortensen et al. (2014) identified different stratigraphic units, including basaltic lavas and hyaloclastite (basalt that contains altered volcanic glass) sequences at shallow (<1.3 km) depth, and dense basaltic dykes at greater depth with little alteration below about 2 km depth. Porosity of corresponding outcrop samples is relatively high, between 11% and 60% (Eggertsson, 2019). We note these compositional differences to the investigated Rodderberg basalt, but regard them as insignificant for the mechanical properties with respect to the highly different mineral content of felsite and the large variability of porosity. Moreover, the behavior of basalt is of general interest for SCGS.

For triaxial deformation experiments on intact rocks we prepared cylindrical samples of 20 mm length and 10 mm diameter with parallel end faces oriented perpendicular to the cylinder axis. For friction tests on split-cylinder

Table 1
Experimental Conditions of Intact Felsite Samples

Sample No.	T °C	Porosity %	stress $_{peak}$ MPa	E GPa	strain $_{peak}$ %	Comment
fels5	25	9.7	264	16	1.9	dry
fels7	160	9.8	327	22	2.9	dry
fels2	300	8.6	357	24	2.1	dry
fels14	300	10.9	274	27	1.4	wet
fels6	400	11.7	303	23	1.7	dry
fels4	500	11.1	265	25	1.6	dry
fels3	700	11.3	206	19	1.3	dry
fels15	700	9.9	323	55	1.1	dry
fels9	800	9.5	293	15	1.1	dry
fels10	900	9.0	325	26	1.5	dry
fels13	900	10.3	117	25	1.1	wet
fels11	1000	9.0	210	17	1.3	dry
fels12	1100	9.8	58	6	4.1	dry

rocks we prepared samples of 22 mm length and 10 mm diameter that contained a split-cylinder oriented at 30° with respect to the axial direction. The surface of the split cylinder in felsite samples were carefully polished with a plastic-bonded cup wheel to prevent multiple breakouts of grains during polishing. Determined root mean square (RMS) surface roughness is 43 ± 15 μm, measured with a white light optical profilometer (Keyence VR-3200) (Table 3). The surfaces of basalt sample saw-cuts were polished using SiC-grains (diameter ≈260 μm), resulting in an RMS roughness of 13 ± 2 μm (Table 4), a procedure that could not be applied to felsite samples because of the risk of breakouts.

All samples were stored in an oven at 50°C (felsite) or 110°C (basalt), regarded as being "dry" in terms of water content. Two felsite samples, fels13 and fels14, were dropped into deionized water for several days before deformation, resulting in 2 vol% added water. Another basalt sample, BASB7 was also dropped into water, yielding 0.2 vol% added water. These three samples are denoted as being "wet" hereafter.

2.2. Methods

The triaxial deformation experiments were performed at constant displacement rate using a Paterson-type gas deformation apparatus, which is provided with an internal load cell (Paterson, 1970). To prevent intrusion of the argon confining pressure medium, samples were sealed by use of thin (0.34 mm) copper jackets, except samples fels11, fels12 and BASB6 that were sealed using thin Fe jackets because of the high temperature applied during testing of these samples. To prevent the jacket from being perforated under confinement, large pores on the outer sample surface, which were artificially created during grinding and polishing, were coated with ceramic adhesive.

Axial strain, ε_e, was calculated from the measured axial displacement using a linear variable displacement transducer (LVDT, Schaevitz DC-E) and subsequently converted to natural strain ε = -ln (1–ε_e), with ε_e = engineering strain, defined positive in compression. For determination of ε_e, axial displacement was corrected for pressure- and temperature-dependent apparatus distortion. For tests on felsite samples, the sample assembly was composed of a combination of alumina and zirconia pistons, requiring a non-linear system compliance correction determined in previous calibration runs. For basalt samples, we applied a linear compliance correction since in these experiments only alumina pistons were used.

To determine axial stress, we corrected the measured axial force for the load supported by the metal sleeve. The strength of the jacket was estimated from calibration runs on copper and iron jackets at high temperature (>400°C) resulting in strength that are quite similar to estimates from power law flow laws for these materials provided by Frost and Ashby (1982). At lower temperature, our measured data for copper creep are poorly sensitive to temperature and pressure matching the low temperature flow law data for obstacle-controlled dislocation glide suggested by Frost and Ashby (1982). Axial (differential) stress, $\Delta\sigma = \sigma_1 - \sigma_3$, was then calculated by subtracting the confining pressure ($P = \sigma_3$) from the corrected axial force, divided by the actual cross-sectional area A of the sample. For intact samples, we assumed constant volume deformation to calculate the strain dependent area A. For split-cylinder samples the change of contact area with increasing axial displacement after yielding (fault reactivation) is given by (Tembe et al., 2010)

$$A/A_0 = \frac{\theta - \sin\theta}{\pi} \text{ with } \theta = \pi - 2\sin^{-1}\left(\frac{\Delta l}{d}\tan\beta\right) \quad (1)$$

where A_0 is initial cross-section area, d is sample diameter and β is the inclination angle of the split-cylinder surface (30°). Here, we assume solely slip of the fault without additional matrix deformation. The associated (uncorrected) shear stress τ and normal stress σ_n acting on the reactivated fault can be calculated from

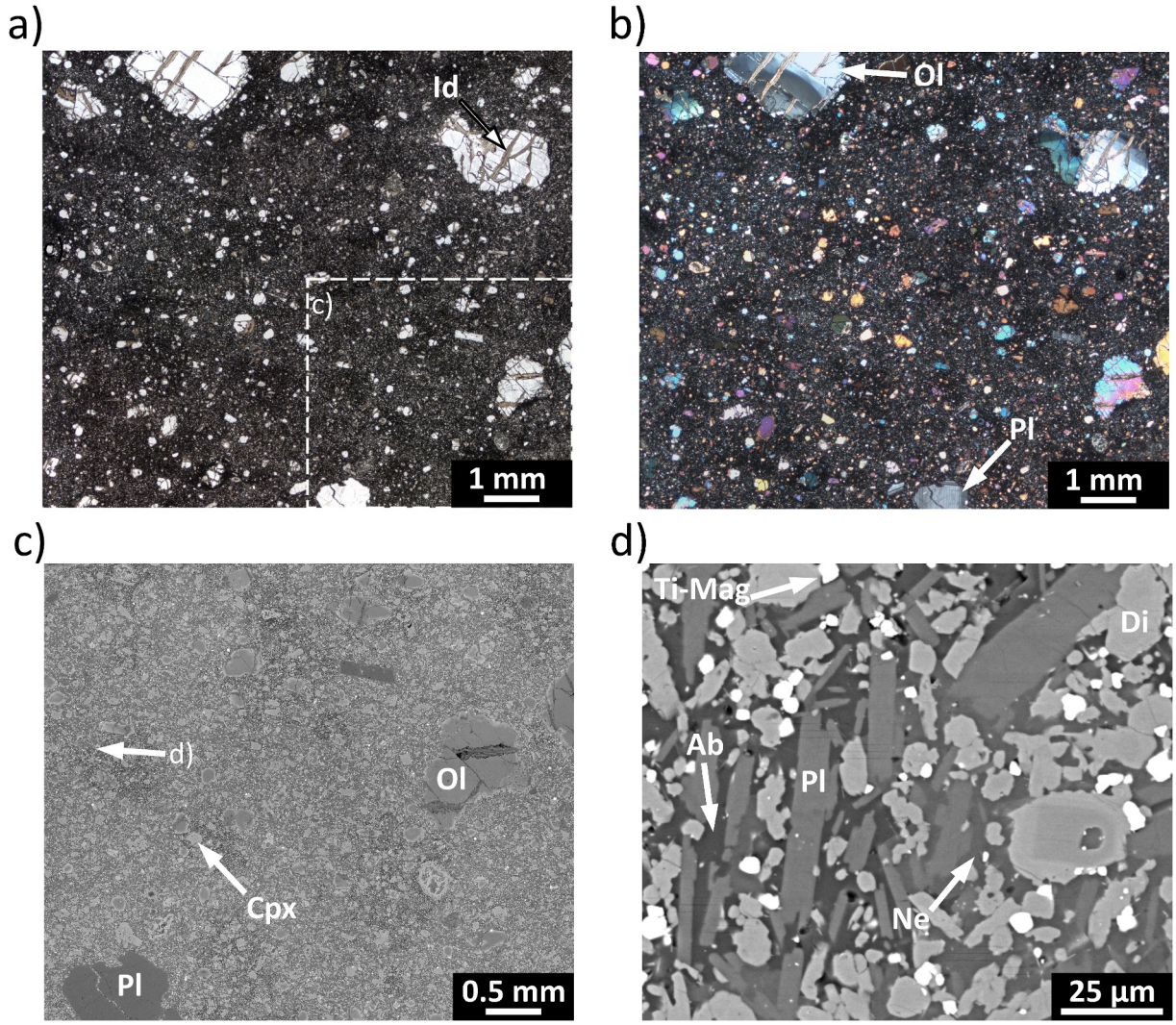

Figure 2. Microphotographs of Rodderberg basalt/basanite shown in plane- (a) and cross-polarized light (b). The area outlined by the dashed line in (a) is further magnified using backscattered electron (BSE) microscopy (c, d). The fine-grained groundmass consists primarily of olivine (Ol), plagioclase (Pl) and clinopyroxene (Cpx) with few phenocrysts (1–3 mm) of the same composition, frequently showing compositional zoning. Olivine phenocrysts show several fractures that are filled with secondary iddingsite (a). BSE analysis of areas with color and brightness variations (a–c) reveals compositional heterogeneity of the minerals filling the interstitial space between microliths, which results from different concentrations of the albite (Ab) and nepheline (Ne) content, respectively (d). Elongated plagioclase and clinopyroxene crystals show a preferred orientation at the microscale (d). Di = diopside, Ti-Mag = titanomagnetite, Qtz Xen = quartz xenocryst.

$$\tau = \tfrac{1}{2}(\sigma_1 - \sigma_3)\sin 2\beta \tag{2}$$

and

$$\sigma_n = \tfrac{1}{2}[(\sigma_1 + \sigma_3) - (\sigma_1 - \sigma_3)\cos 2\beta] \tag{3}$$

The true shear and normal stress are derived by dividing the uncorrected data by the factor A/A_0.

The shear strength as a function of the normal stress acting on the surface can be described by the Mohr-Coulomb friction criterion

$$\tau = c + \mu\sigma_n \tag{4}$$

Table 2
Experimental Conditions of Intact Basalt Samples

Sample No.	T °C	Porosity %	stress $_{peak}$ MPa	E GPa	strain $_{peak}$ %	Comment
BASB1	20	0.6	>837	78	1.1	dry
BASB2	300	0.6	747	70	1.3	dry
BASB3	500	0.4	517	52	1.0	dry
BASB8	500	0.3	421	61	1.8	dry
BASB4	700	0.4	520	28	2.1	dry
BASB7	700	0.4	269	16	2.8	wet
BASB5	900	0.4	160	15	8.8	dry
BASB6	1100	0.5	≈1	0.3	1.5	dry

where μ is the friction coefficient and c is cohesion. If cohesion is negligible, the frictional resistance μ_r is given by Amonton's law

$$\mu_r = \tau/\sigma_n \quad (5)$$

Accuracy of axial stress is expected to be better than about 4% and 10% for intact and split-cylinder samples, respectively. Temperature was measured using a thermocouple (1% accuracy) positioned about 3 mm above the top of the samples. Calibration runs with hollow dummy samples revealed a temperature gradient along the sample of less than 3°C. Sampling rate of the data acquisition system was 1 Hz.

After deformation, we prepared thin sections oriented parallel to the long axis of the samples and perpendicular to the developed fault plane. Microstructural analysis was done by optical microscopy (OPM, Leica DMC4500). Some samples were additionally inspected using a scanning electron microscope (SEM) on polished and carbon-coated sections at 20 kV acceleration voltage and 10 mm working distance. Composition analysis was done using an attached energy-dispersive X-ray analyzer (EDX). High resolution investigations on focused ion beam (FIB) prepared sections of selected samples were done with a transmission electron microscope (TEM, FEI Tecnai).

3. Results

3.1. Mechanical Data

In total, we performed 13 triaxial compression tests on intact felsite samples (Table 1) and 8 tests on intact basalt samples (Table 2) at 50 MPa confining pressure and temperatures between 25 and 1100°C. Split-cylinder friction tests were done on 10 felsite samples at T = 20–900°C, P = 30–70 MPa (Table 3) and on 19 basalt samples at T = 20–700°C, P = 30–90 MPa (Table 4). All tests were performed at constant axial displacement velocity, corresponding to an axial strain rate of about 4.5–5 × 10^{-5} s^{-1}.

3.1.1. Stress-Strain Behavior and Peak Strength of Intact Samples

Individual intact samples were deformed at constant temperature and displacement rate, and a fixed confining pressure of 50 MPa, representative for the lithostatic pressure at about 2 km depth, that is, close to the pressure conditions at the top of the magma chamber at Krafla. Felsite samples deformed mostly in a ductile manner, that is, they showed pronounced post peak deformation and in many cases strain weakening behavior in the post peak stress regime with strongest weakening at T = 300°C and minor weakening at the highest temperatures (Figure 3a). Peak differential stress of dry samples varied between about 60 and 360 MPa, depending on temperature, with the lowest value measured at 1100°C (Figure 4). Reproducibility of peak stress is relatively poor (e.g., difference in peak stress is 117 MPa; 206 MPa for sample fels3 and 323 MPa for fels15), measured at T = 700°C and is probably associated with porosity variations (Table 1, Figures 3a and 4). Peak strains were between 1.9% and 4.1% (Table 1) and roughly estimated Young's moduli are in the range of 6–55 GPa, both with no clear temperature dependence. However, the accuracy of determined Young's modulus is very limited due to the uncertainty of jacket strength and system stiffness corrections. The wet samples fels13 and fels14 were distinctly weaker (≈1.3 × at 300°C and 2.8 × at 900°C) than the corresponding dry samples. Note that the test conditions were undrained, that is, pore pressure was not controlled, which does not allow for effective stress estimation.

At temperatures up to 700°C, intact basalt samples showed brittle behavior without a clear yield point before sudden failure (Figure 3b). Sample BASB1 deformed at room temperature was terminated before failure to prevent damage of the used assembly. Therefore, the real peak strength is somewhat higher than 837 MPa labeled in Table 2, indicated in by dotted lines in Figures 3b and 4.

For one sample deformed at 500°C (BASB8) strength was recovered after a first stress drop with subsequent slight weakening. In contrast, at T = 900°C we observed almost steady state stress up to about 16% strain. At the

Table 3
Frictional Properties of Saw-Cut Felsite Samples

Sample no.	S_q μm	T °C	P MPa	$\Delta\sigma_{yp}$ MPa	$\Delta\sigma_{ip}$ MPa	μ_{r_yp}	μ_{r_ip}	$\mu_{r\_yp\_ave}$	$\mu_{r\_ip\_ave}$	μ_{yp}	c_{yp} MPa	μ_{ip}	c_{ip} MPa
fels_s02	36	25	30	21	78	0.26	0.68	0.40	0.68	0.55	−7.8	0.69	−0.5
			50	82	130	0.50	0.68						
			70	95	184	0.44	0.69						
fels_s09	20	200	30	45	98	0.47	0.78	0.48	0.75	0.39	6.9	0.68	6.2
			50	94	154	0.55	0.75						
			70	90	200	0.42	0.72						
fels_s06	43	300	50	110	178	0.61	0.82						
fels_s03	34	300	30	91	105	0.75	0.81	0.62	0.81	0.21	31.3	0.83	0.1
			50	102	177	0.58	0.81						
			70	112	246	0.49	0.81						
fels_s05	76	450	30	57	144	0.56	0.94	0.54	0.91	0.48	3.8	0.83	9.3
			50	90	221	0.54	0.91						
			70	118	286	0.51	0.88						
fels_s07	40	600	30	60	131	0.58	0.90	0.53	0.91	0.31	14.9	0.95	0.2
			50	95	228	0.56	0.92						
			70	94	308	0.44	0.91						
fels_s01	57	700	50	–	–	0.01	0.01						
fels_s08	33	700	30	63	103	0.60	0.80	0.57	0.84	0.47	6.6	0.95	−6.7
			50	102	187	0.58	0.84						
			70	123	280	0.53	0.87						
fels_s04	50	750	30	65	95	0.61	0.77	0.57	0.79	0.37	11.7	0.87	−4.4
			50	86	171	0.52	0.80						
fels_s11	34	800	30	46	101	0.48	0.79	0.23	0.33				
			50	*23*	*23*	0.18	0.18						
			70	*4*	*4*	0.02	0.02						
fels_s10	46	900	30	59	71	0.57	0.64	0.22	0.25				
			50	*11*	*11*	0.09	0.09						
			70	*2*	*2*	0.01	0.01						

Note. S_q = (RMS) roughness, T = temperature, P = pressure, $\Delta\sigma_{yp}$ = differential stress at yield point, $\Delta\sigma_{ip}$ = differential stress at intersection point, μ_{r_yp} = frictional resistance at yield point, μ_{r_ip} = frictional resistance at intersection point, $\mu_{r\_yp\_ave}$ = average frictional resistance at yield point, $\mu_{r\_ip\_ave}$ = average frictional resistance at intersection point, μ_{yp} = friction coefficient at yield point, c_{yp} = cohesion at yield point, μ_{ip} = friction coefficient at intersection point, c_{ip} = cohesion at intersection point.

highest temperature of 1100°C the strength is almost negligible (Table 2, Figure 3b). For this particular sample, we observed a temperature anomaly at the bottom winding of the furnace and increased barreling of the lower sample part, indicating that the temperature at the sample bottom was possibly higher than 1100°C. The wet sample BASB7 also showed some strain weakening after the first stress drop and the peak strength is about 1.9 times lower than of the dry sample BASB4, both deformed at T = 700°C.

Peak strength of the basalt decreases almost continuously with increasing temperature (Figure 4). Compared to the felsite sample, the basalt is considerably stronger at temperatures up to 700°C. Above about 800°C the felsite appears to be stronger than the basalt. Note, however, that the reproducibility of peak strength is fairly poor (about 36% at 700°C for felsite and 20% for basalt at 500°C, see Figure 4).

Table 4
Frictional Properties of Saw-Cut Basalt Samples

Sample No.	S_q μm	T °C	P MPa	$\Delta\sigma_{yp}$ MPa	$\Delta\sigma_{ip}$ MPa	μ_{r_yp}	μ_{r_ip}	$\mu_{r\_yp\_ave}$	$\mu_{r\_ip\_ave}$	μ_{yp}	c_{yp} MPa	μ_{ip}	c_{ip} MPa	Porosity %
BAS20	12	25	30	67	79	0.62	0.69	0.53	0.63	0.38	10.7	0.44	13.3	1.7
BAS08	13	25	50	77	113	0.48	0.63							1.2
BAS21	12	25	70	111	133	0.49	0.56							1.5
BAS16	12	300	30	56	70	0.55	0.64	0.53	0.60	0.50	3.0	0.51	8.9	1.9
BAS05	13	300	50	92	131	0.54	0.69							0.7
BAS15	13	300	70	123	130	0.53	0.55							5.3
BAS19	13	300	90	170	186	0.56	0.59							2.3
BAS22	13	300	90	136	171	0.47	0.56							0.2
BAS11	13	500	30	78	100	0.68	0.79	0.52	0.64	0.42	8.5	0.47	0.6	1.7
BAS06	10	500	50	59	95	0.40	0.56							0.1
BAS12	14	500	70	125	167	0.53	0.65							0.9
BAS17	13	500	90	139	174	0.48	0.56							2.7
BAS07	11	600	50	84	115	0.51	0.63	0.42	0.51					0.1
BAS10	17	600	50	47	58	0.33	0.39							3.5
BAS14	12	700	30	9	18	0.12	0.23	0.21	0.25	0.07	11.0	0	19.1	6.9
BAS09	14	700	50	52	62	0.36	0.41							4.1
BAS13	14	700	70	45	46	0.24	0.25							7.2
BAS18	13	700	90	21	23	0.10	0.10							1.2
BAS04	12	700	50	<1	<1	<0.01	<0.01							0.4

Note. S_q = (RMS) roughness, T = temperature, P = pressure, $\Delta\sigma_{yp}$ = differential stress at yield point, $\Delta\sigma_{ip}$ = differential stress at intersection point, μ_{r_yp} = frictional resistance at yield point, μ_{r_ip} = frictional resistance at intersection point, $\mu_{r\_yp\_ave}$ = average frictional resistance at yield point, $\mu_{r\_ip\_ave}$ = average frictional resistance at intersection point, μ_{yp} = friction coefficient at yield point, c_{yp} = cohesion at yield point, μ_{ip} = friction coefficient at intersection point, c_{ip} = cohesion at intersection point.

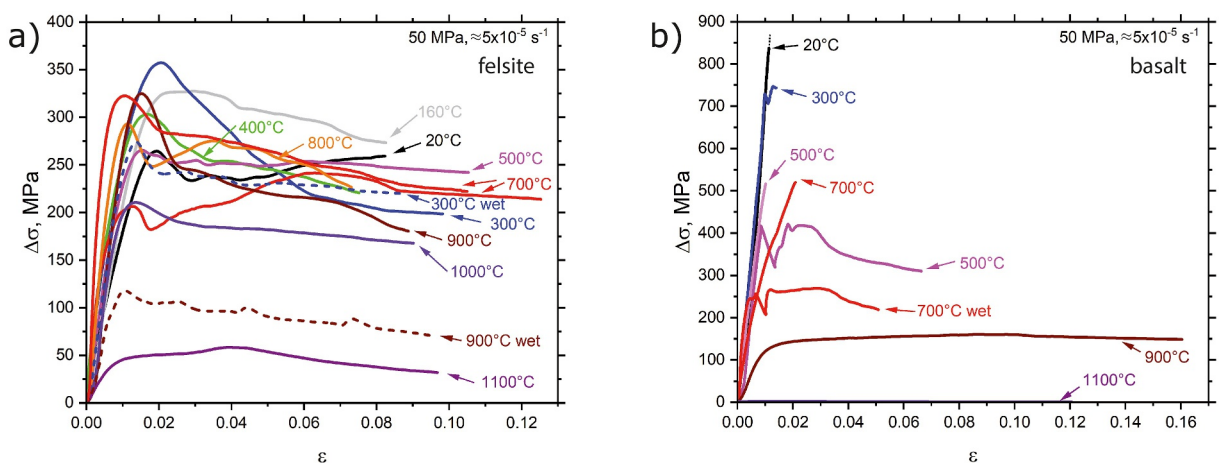

Figure 3. Stress versus strain curves of intact felsite (a) and basalt (b) samples, all deformed at $P = 50$ MPa confining pressure and an axial strain rate of 5×10^{-5} s^{-1}. Samples were tested under "dry" conditions unless noted as "wet." Most felsite samples show strain weakening after peak stress, whereas basalt samples were more brittle at low temperature. Temperatures are labeled on each curve.

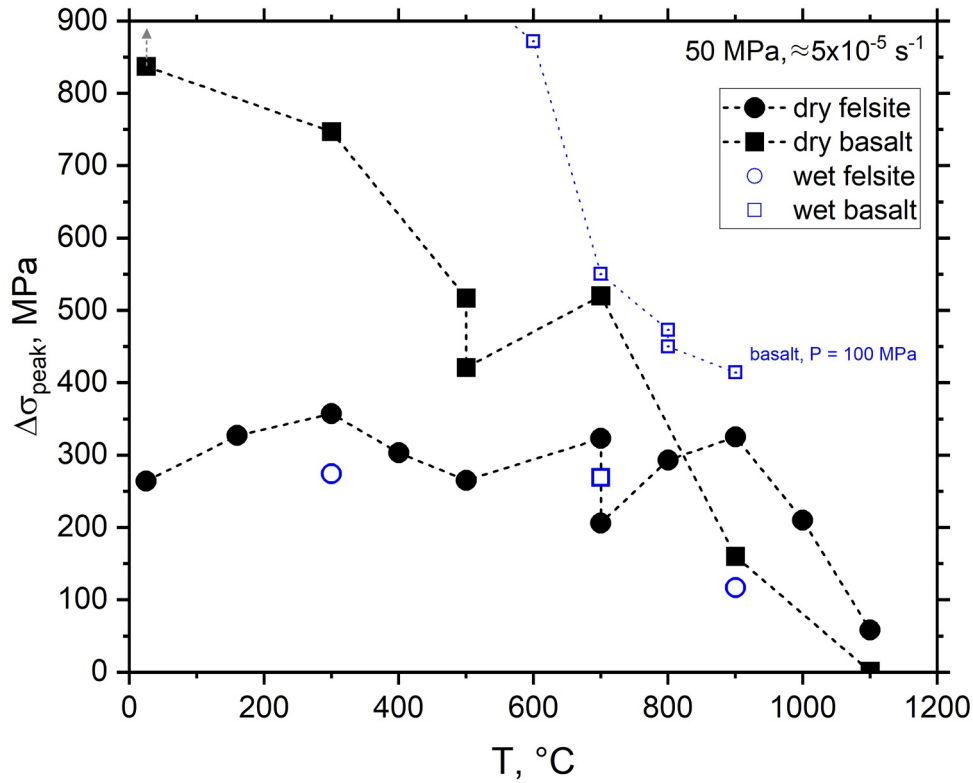

Figure 4. Variation of peak strength of intact felsite (circles) and basalt (squares) samples with temperature, measured at a strain rate of $\approx 5 \times 10^{-5}$ s^{-1}. Strength of wet Languedoc-Roussillon basalt at an effective pressure of 100 MPa and a strain rate of 1×10^{-5} s^{-1} was determined by Violay et al. (2012). Solid and open symbols represent dry and wet samples, respectively.

3.1.2. Stress-Strain Behavior of Saw-Cut Samples

Because of the limited amount of felsite starting material available, split-cylinder tests on this rock type were in most cases conducted in runs with a stepwise increase in confining pressures of 30, 50, and 70 MPa to allow determination of the friction coefficient μ by applying the Mohr-Coulomb criterion (Equation 4). Some samples were additionally deformed in a second run starting again at 30 MPa pressure (not shown here), which generally showed a higher strength and a higher transition stress from elastic to inelastic behavior compared to the first runs, indicating increasing compaction. Applied axial strain rate was 5×10^{-5} s^{-1} and maximal axial strain of each run was about 1% at fixed temperatures between 25 and 900°C (Table 3). At almost all investigated temperatures up to 750°C, the strength of split-cylinder samples increased with increasing confinement with maximum values ≤320 MPa (Figures 5a–5g). Conversely, at $T = 800$ and 900°C the strength decreased with increasing P (Figures 5g and 5h).

Generally, samples showed stable sliding with strain hardening behavior after yielding. At each confining pressure, we performed one or two unloading and reloading cycles. For better readability, most of the unloading/reloading data are skipped in Figure 4 except in Figure 4a, where they are shown as thin lines. Interestingly, after reloading the samples exhibited unstable slip events after reaching the previous stress level, at which unloading was initiated. The magnitude of these stress drops is between 3 and 29 MPa, mostly increasing with pressure and temperature, but they disappeared at $T \geq 700$°C (Figures 5f and 5g).

At $T = 300$°C, we repeated one run at 50 MPa pressure up to a high strain of about 4.5% without unloading cycles (sample fels_s06), yielding a fairly good reproducibility in terms of yield stress and strain hardening, but lower Young's modulus (Figure 5c). One sample (fels_s01) deformed at $T = 700$°C and $P = 50$ MPa showed an almost negligible strength (Figure 5f).

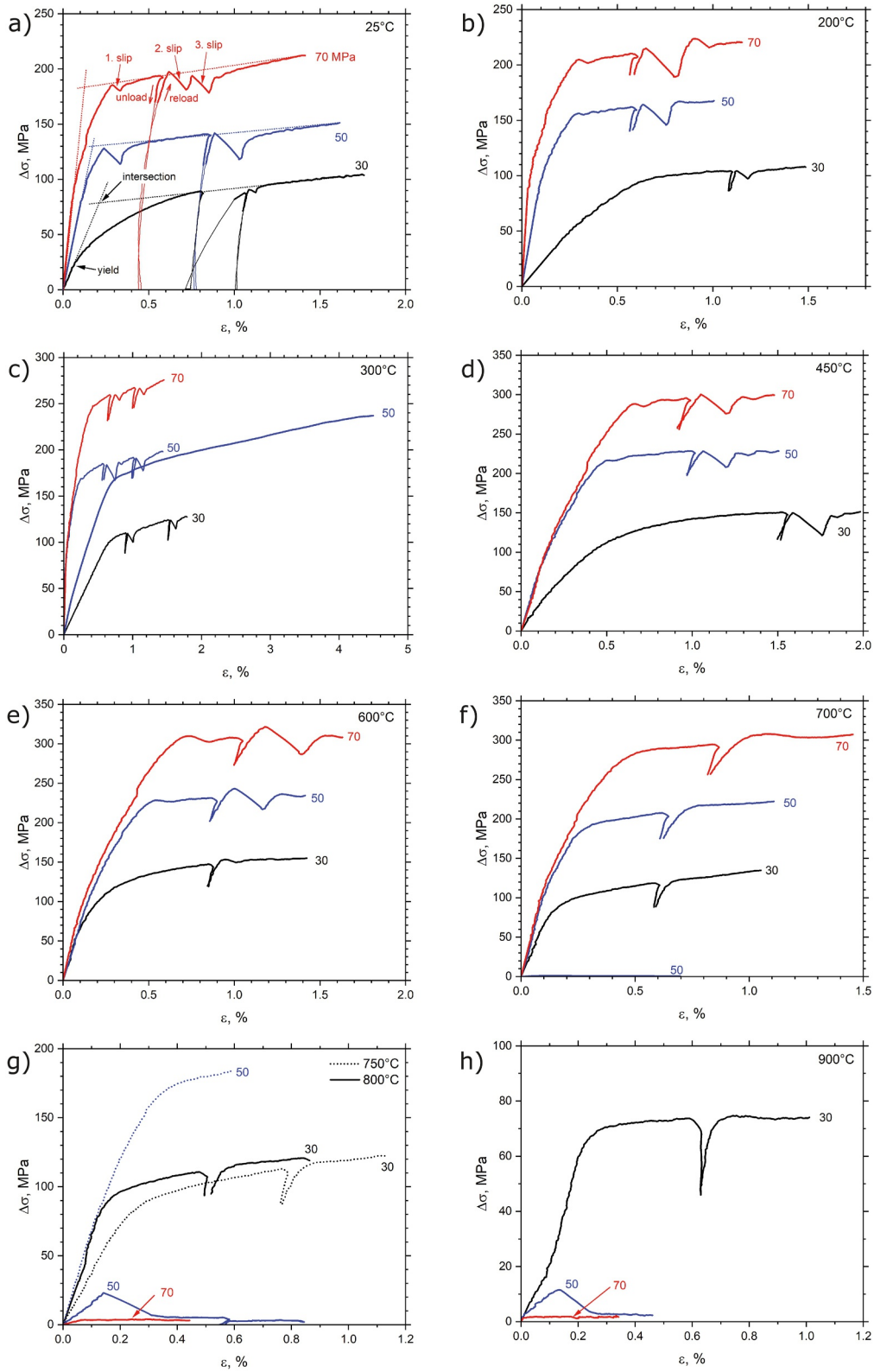

Figure 5.

Basalt samples were deformed at temperatures of 25–700°C in a single run at constant axial strain rate of $\approx 4.5 \times 10^{-5}$ s^{-1} to axial strains of about 4%–6%. Confining pressure varied between 30 and 90 MPa (Table 4, Figure 6). Most samples showed a poorly defined yield point after initial elastic loading and subsequently stable sliding with strain hardening after about 0.2 to 0.4% strain, similar to felsite. Often, but not always, strength increases with pressure at given temperature. At $T = 700$°C two samples deformed at $P = 50$ and 70 MPa exhibited strain weakening after peak stress and samples were distinctly weaker than at $T \leq 500$°C (Figure 6d). One sample deformed at 50 MPa pressure and 700°C temperature (BAS04) showed minor strength.

3.1.3. Frictional Properties

From the measured stress-strain curves we derived the frictional properties of felsite and basalt at elevated temperatures. The friction coefficient μ can be determined from Equation 4 by plotting the shear stress versus normal stress at constant temperature and different pressures, where the slope of a linear least square fit equals μ and the offset is the cohesion c. Alternatively, the data can be plotted in a differential stress versus confining pressure diagram, where the offset at $P = 0$ is the uniaxial compressive strength UCS, that is,

$$\Delta\sigma = \mathrm{UCS} + rP \tag{6}$$

The slope r obtained from linear regression analysis is related to μ by (e.g., Baud et al., 2014; Zoback, 2007)

$$r = \left[\sqrt{\mu^2 + 1} + \mu\right]^2 - 1 \tag{7}$$

or

$$\mu = \frac{r}{2\sqrt{r+1}} \tag{8}$$

and UCS can be determined from cohesion c by

$$\mathrm{UCS} = 2c\sqrt{r+1} \tag{9}$$

We assume that the yield point ($\Delta\sigma_{yp}$) represents the onset of frictional sliding, termed initial friction (e.g., Byerlee, 1978). However, the used sample assembly and deformation apparatus, which requires relatively severe force corrections due to the metal jacket, did not allow for a precise determination of the yield stress and for elastic stiffness. Since we observed stable sliding with continuous hardening in most of our friction experiments, we were not able to define a peak (maximum) friction value. Instead, we determined the intersection point ($\Delta\sigma_{ip}$) between extrapolated elastic deformation and extrapolated linear hardening behavior, defined in the following as "intersection friction." One example is shown in Figure 5a for the first run at $P = 30$, 50 and 70 MPa (dotted lines).

For felsite samples both the yield stress and the stress at the intersection point ("intersection stress") increase with confinement except at $T \geq 800$°C (Figure 7, Table 3). Linear regression of the data at individual temperatures allows to determine the slope r and uniaxial compressive strength UCS (Equation 6), from which the friction coefficient μ and the cohesion c can be derived (Equations 8 and 9, respectively). The resulting friction coefficients μ_{yp} for the yield point vary between 0.21 and 0.55 and the associated cohesion values, c_{yp}, between ≈4 and 31 MPa, neglecting the 25°C data (Table 3). A typical error bar is about 0.06 and ≈ 2 MPa for μ_{py} and c_{yp}, respectively. Taking the intersection point, the friction coefficient μ_{ip} ranges between 0.68 and 0.95 (Table 3), often distinctly higher than μ_{py}. Neglecting (unrealistic) negative values, the corresponding cohesion is $c_{ip} \approx 0.1$–9.3 MPa (Table 3). Using Equations 2 and 3 the frictional resistance at the yield point (μ_{r_yp}) and the

Figure 5. Stress strain curves of felsite saw-cut samples deformed at $T = 20$°C (a), 200°C (b), 300°C (c), 450°C (d), 600°C (e), 700°C (f), 750°C and 800°C (g), and 900°C (h). Curve labeling indicates applied confining pressure varying from 30 to 70 MPa. All tests were performed at an axial strain rate of about 5×10^{-5} s^{-1}. The low stress part of the unloading/reloading cycles are skipped for better readability, except in (a), where they are shown by thin lines. Slip events are exemplarily indicated by arrows at 20°C temperature and 70 MPa pressure in (a). For the evaluation of frictional properties, we determined the yield point (initial friction) and the intersection point between extrapolated elastic and strain hardening behavior (intersection friction), indicated by dotted lines in (a). Note different scales.

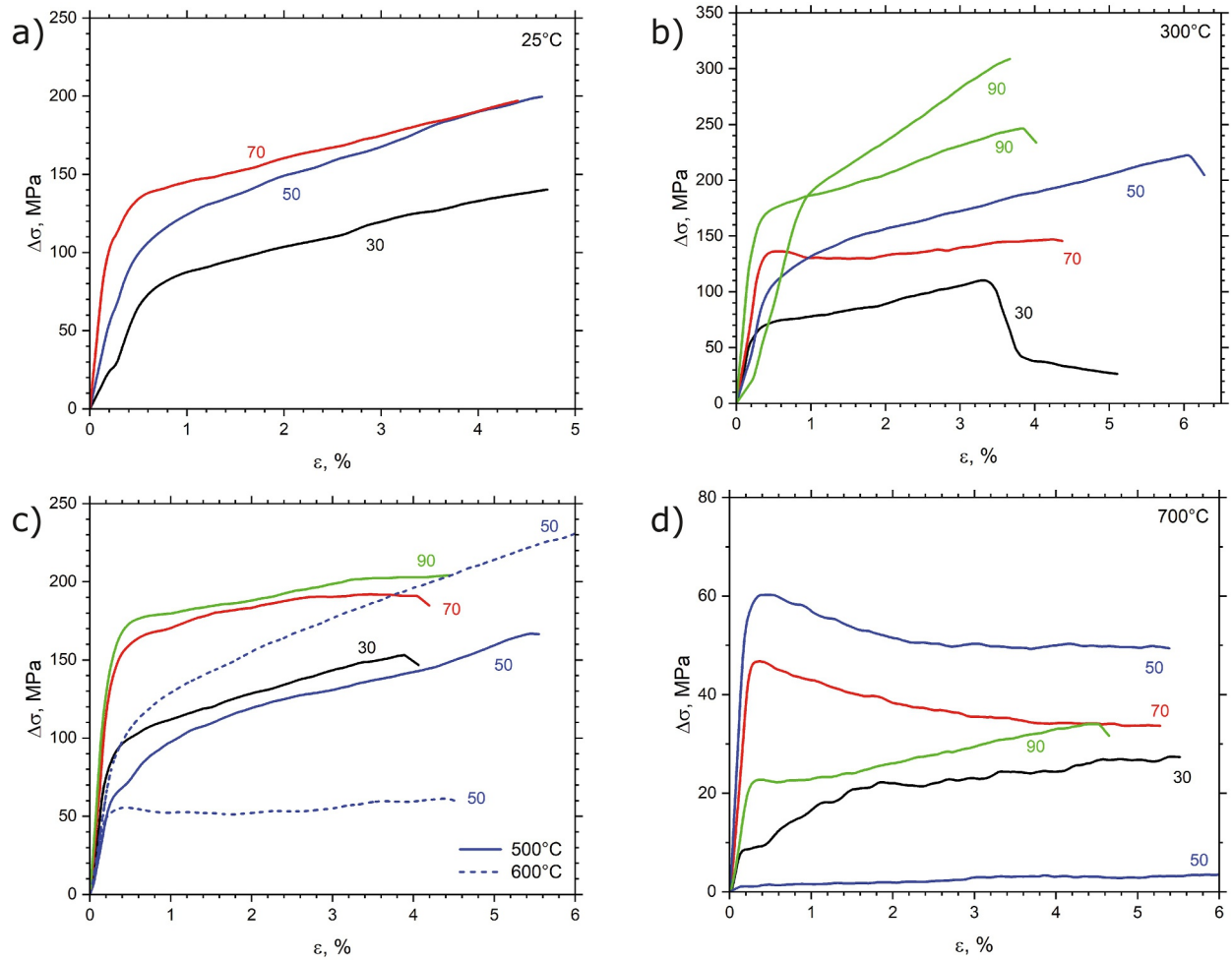

Figure 6. Stress strain curves of basalt saw-cut samples deformed at $T = 20°C$ (a), 300°C (b), 500°C and 600°C (c), and 700°C (d). Curve labeling indicates applied confining pressure. All tests were performed at an axial strain rate of about 4.5×10^{-5} s^{-1}. Note different scales.

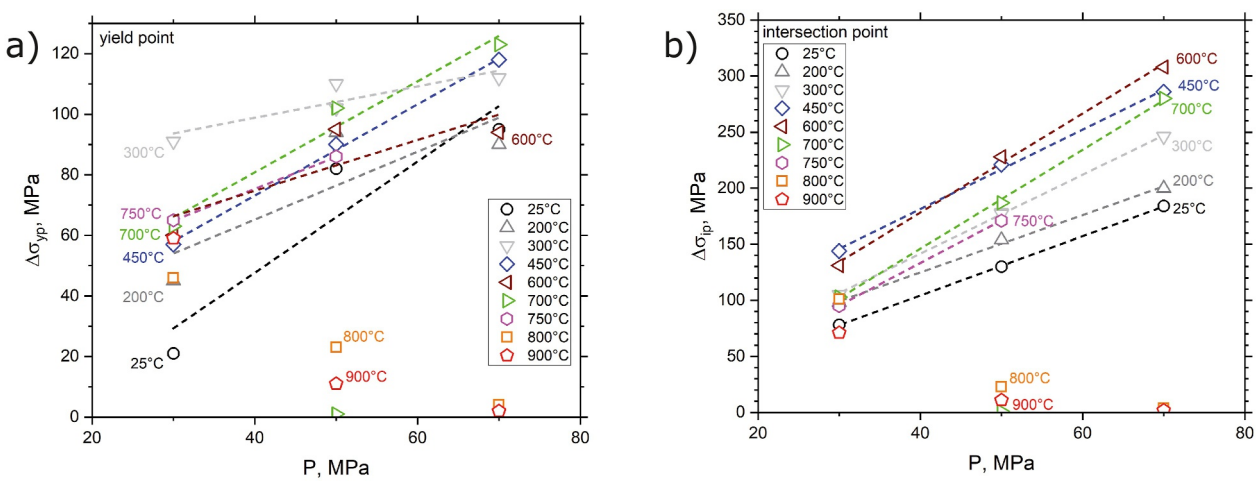

Figure 7. Differential stress at the yield point (a) and at the intersection point (b) of felsite saw-cut samples. Dotted lines represent least square fits to the data at fixed temperatures ≤750°C.

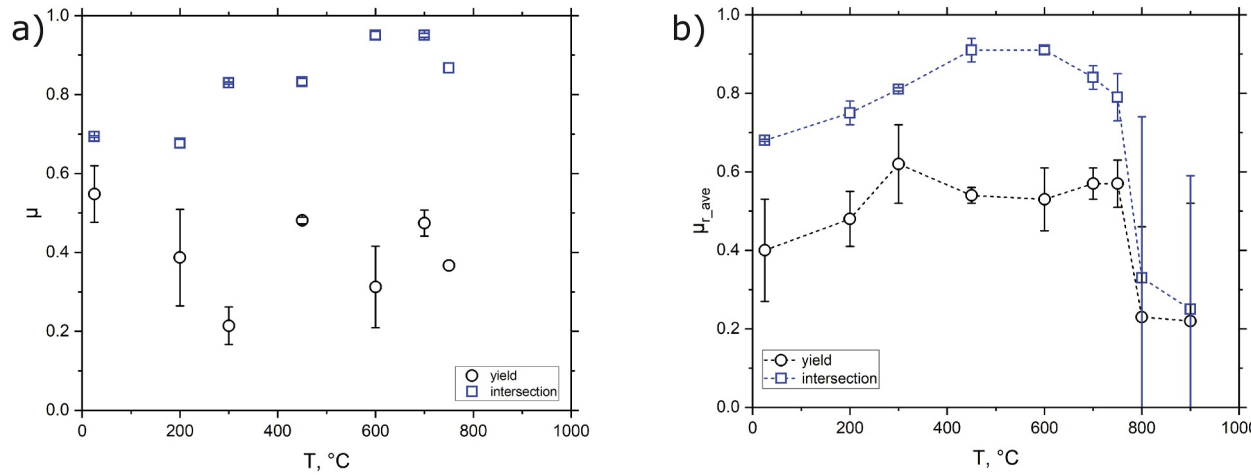

Figure 8. Variation of friction coefficient μ (a) and mean frictional resistance μ_{r_ave} (b) with applied temperature for felsite split-cylinder samples, determined from the yield and intersection point.

intersection point (μ_{r_ip}) can be calculated from $\Delta\sigma_{yp}$ and $\Delta\sigma_{ip}$, respectively. Values vary between 0.01 and 0.94 (Table 3), with a typical error bar of about 0.11. At each temperature we additionally determined the mean frictional resistance by averaging all data obtained at pressures between 30 and 70 MPa, resulting in values of $\mu_{r\_yp\_ave} = 0.22$–0.62 for the yield point and $\mu_{r\_ip\_ave} = 0.25$–0.91 for the intersection point (Table 3).

Regarding initial friction at the yield point, μ and c values both show some scatter and reveal no systematic change with temperature up to 750°C, but a slight increase with T for intersection friction (Figure 8a). Cohesion c appears to be independent of temperature (Figure A1a). Similar to μ, the mean frictional resistance μ_{r_ave} at the intersection point is considerably higher than determined at the yield point and drops to low values of about 0.22 at $T \geq 800$°C (Table 3, Figure 8b).

The basalt split-cylinder samples also show an increase of yield and intersection stress with pressure (Figure 9). Calculated yield (initial) friction coefficient (μ_{yp}) lies between 0.07 and 0.50 and intersection friction coefficient (μ_{ip}) between 0 and 0.51 (Table 4) with an uncertainty of ≈0.12, deduced from the slope of least square regression analysis (Figure 9). The corresponding cohesion values range from 3 to 11 MPa for yield friction and from ≈1 to 19 MPa for intersection friction (Table 4) with a relatively large average error of about 10 MPa. The associated frictional resistance is between 0.10 and 0.68 for the yield point with average values for each temperature between

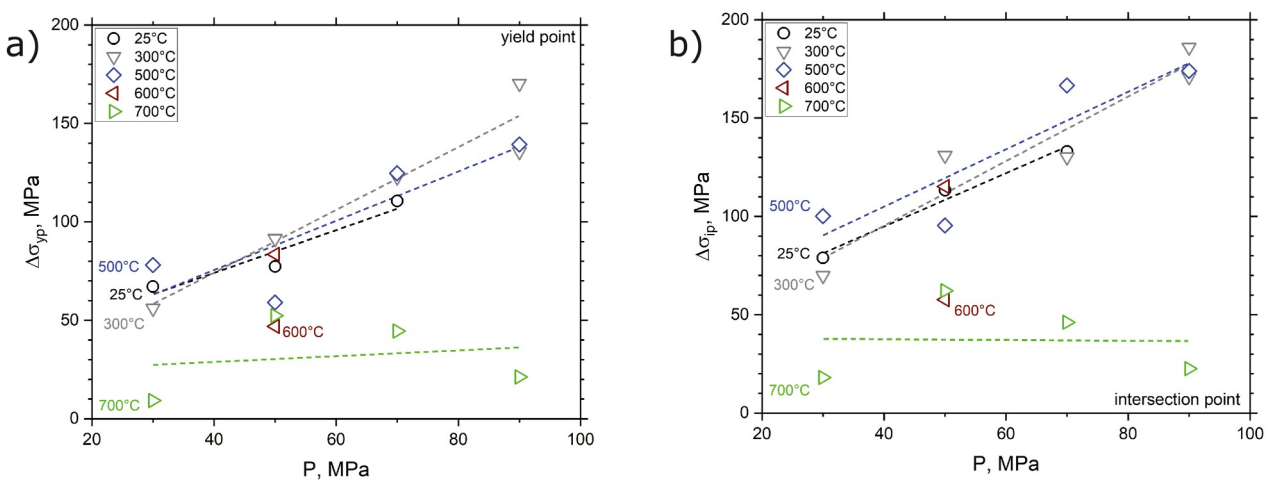

Figure 9. Differential stress at the yield point (a) and intersection point (b) of basalt saw-cut samples. Dotted lines represent least square fits to the data at fixed temperatures ≤700°C.

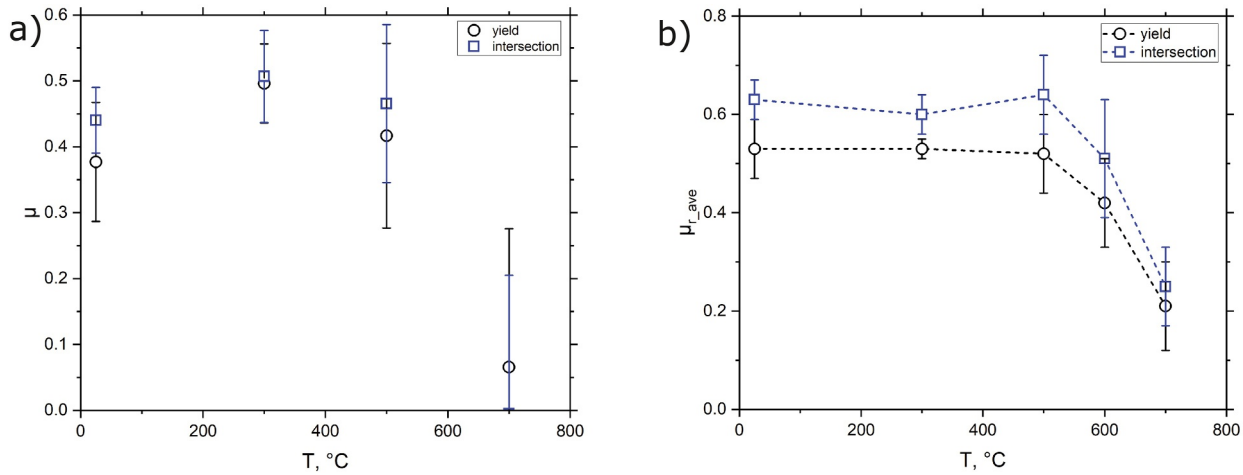

Figure 10. Variation of friction coefficient μ (a), mean frictional resistance μ_{r_ave} (b) with applied temperature for basalt saw-cut samples, determined from the yield and intersection point.

0.21 and 0.53 and a typical uncertainty of ≈0.07 (Table 4). For the intersection point the frictional resistance μ_{r_ip} is ranging from 0.1 to 0.79 and mean values $\mu_{r\_ip\_ave}$ range from 0.25 to 0.64 (Table 4).

The friction coefficient and frictional resistance of basalt are both relatively insensitive to temperature up to 500°C, above which they decrease (Figure 10). The intersection friction is slightly higher (<0.1) than the initial friction and the difference between μ_r and μ is larger for the intersection point compared to the yield point (Table 4, Figure 10). Cohesion is higher for intersection friction than for initial friction (see appendix, Figure A1b).

3.2. Microstructures

To analyze post-deformation microstructures, samples were embedded in blue epoxy resin and sectioned perpendicular to the macroscopically visible shear plane (where present) and parallel to the σ_1-direction using a low-speed diamond saw. Intact samples exhibit a wide range of deformation features that systematically evolve with increasing temperature, reflecting a transition from discrete, brittle shear fractures at lower temperatures (≤800°C for felsite, and <700°C for basalt) to progressively more ductile, that is, distributed deformation, and likely melt-enhanced flow at the highest applied temperatures.

3.2.1. Deformed Felsite

At temperatures lower than 800°C and independent of water content, deformation of intact felsite samples is highly localized along brittle fault zones resulting in large portions of the samples remaining almost undeformed. The fault zones are characterized by melt-free cataclastic flow along shear fractures and are accompanied by a marked increase in porosity after deformation (see appendix, Figures A2a–A2d). Developed fault zones commonly contain multiple shear planes, which exhibit non-planar geometries, resulting in anastomosing structural patterns. Shear fractures are characterized by angular mineral fragments with a broad grain size distribution (submicron to several tens of micrometer), showing a high density of transgranular tensile microcracks and pervasive grain crushing and comminution (Figure 11a). The boundary between shear zone and wall rock is often poorly defined, and commonly overprinted by extensive off-fault damage zones. These damage zones can extend up to 500 μm from the main shear plane, and show temperature-invariant geometries up to 800°C. Within the fault zones, principal slip planes exhibit a significant grain size reduction and are dominated by the finest grains (submicron-sized), reflecting strain localization (Figure 11a). Due to the heterogeneous nature of the felsite, pre-existing macropores significantly influence the morphology of fractures and crack propagation. When intersected by shear fractures, these pores often collapse, resulting in localized widening of the damage zone. Outside of the main deformation zones, porosity generally remains preserved.

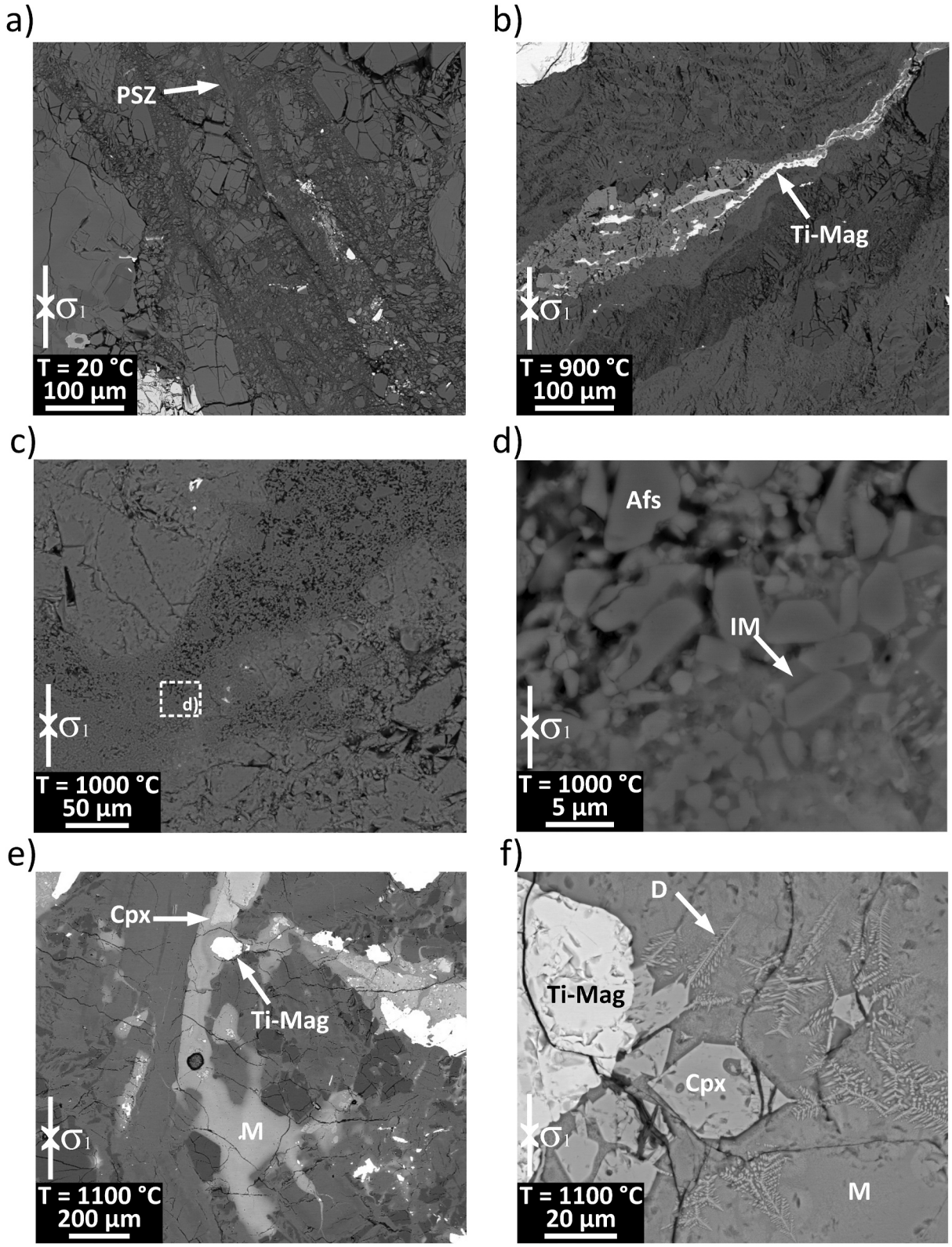

Figure 11.

Above 800°–900°C, increased bulging of the recovered samples suggests a greater contribution of distributed microcracking than slip along discrete shear planes. Furthermore, relative to samples that experienced temperatures <800°C (Figures A2a–A2d), macroscopic deformation changes markedly from localized to fully distributed (cf. Figures A2e–A2h). In addition, samples deformed beyond 800°C exhibit lower porosity than the starting material, suggesting a reduced contribution of brittle deformation mechanisms to the overall strain. In the sample deformed at 900°C under dry conditions (Figure A2e), a discrete shear band developed in the absence of significant damage around the fault zones. The shear zone exhibits microstructures indicative of combined cataclastic and granular flow, and locally, titanomagnetite grains show elongated flow structures along shear direction (Figure 11b). In some regions, well-rounded, spheroidal grains are embedded in material resembling quenched melt (e.g., Figure 11d). The presence of quenched melt is further supported by a brownish discoloration of the matrix in plane-polarized light, which becomes increasingly prevalent with increasing temperature (Figures A2e–A2f). Furthermore, Masotta et al. (2018) observe the onset of partial melting, which was determined through chemical variations between felsite bulk and felsite glass, at around 950°C. Under wet conditions at 900°C, no discrete shear zones developed; instead, deformation is homogeneous (Figure A2f).

Similar features are observed in samples that experienced deformation at 1000°C under dry conditions. Partial melting becomes evident and deformation is no longer localized in discrete fractures, but instead distributed across larger volumes of the rock. Melting appears to be localized in zones that underwent extensive grain comminution as further shown by the pervasive discoloration seen in plane polarized light (Figures A2f–A2h).

At 1100°C, the sample exhibits clear and pervasive evidence of partial melting (Figures 11e and 11f). A dramatic reduction in porosity is observed alongside with extensive, widespread brownish glass in the matrix (Figure A2h). Deformation is primarily accommodated by viscous flow within a partially molten matrix without any significant contribution of microcracking (Figure 11e). Partial melting produces sub-to well-rounded grains with augite commonly producing reaction rims due to resorption. Well-developed dendritic structures of clinopyroxene at the edges of molten crystals or within the glass indicate rapid crystallization from an undercooled melt (Figure 11f). In partially molten samples, the melt compositions are relatively consistent and suggest that melting mainly involved Fe–Mg–Ca-bearing mafic minerals, including clinopyroxene and titanomagnetite/ilmenite. Consequently, the resulting melt is enriched in Fe, Mg, Ca, and K, compared to the initial material, while quartz and sodic plagioclase persisted as solid phases.

Thin sections of deformed saw-cut samples show distinct shearing along the predefined fault planes, except sample fels10 deformed at the highest temperature of 900°C, which reveal minor barreling. SEM imaging of the saw-cut planes reveals that, at temperatures up to 300°C, shear is primarily accommodated by cataclastic flow (Figure 12a), with deformation structures similar to those observed in deformed intact samples. Therefore, a layer of porous gouge up to 75 μm width, consisting of angular mineral fragments of various grain sizes, developed from tensile cracking, rigid grain rotation, and grain comminution. This leads to a distinct reduction/gradient in grain size toward the principal slip zone, which experienced the most shear strain. However, in contrast to intact samples, no off-fault damage zone adjacent to the saw-cut surfaces developed.

At temperatures up to 650°C, besides cataclastic gouge, we also observe the formation of nanograins (Figure 12b) as well as a low-porous, chemically heterogeneous potentially amorphous material appearing in flow structures (Figure 12c–12d). Within these layers (usually <40 μm in thickness), containing occasionally vesicles, no individual grains can be distinguished. As temperature increases, the contribution of cataclasis reduces notably, as the amount of the potentially amorphous material compared to cataclastic gouge increases.

At temperatures above 650°C, indicators of deformation are barely visible on the SEM scale as samples appear as the starting material (Figure 12f). In the absence of any cataclastic processes, we observe the formation of a μm-thick layer of potentially amorphous material containing vesicles as well as embedded spherical, sub-rounded

Figure 11. BSE-images of felsite samples, showing details of deformation microstructures across applied temperatures. Up to 800°C (a), deformation is accommodated by cataclastic flow within fault zones, where strain localizes along principal slip zones (PSZ) composed of densely comminuted mineral fragments. At higher temperatures (b), shear zones develop, exhibiting reduced porosity and distributed microcracking. At 1000°C (c, d), partial melting governs the deformation behavior. Sub-rounded grains are enveloped by interstitial melt (IM), providing evidence for melt-lubricated grain boundary sliding. At 1100°C (e, f), deformation is dominated by melt-assisted flow characterized by an interconnected melt network (M). Dendritic (D) clinopyroxene and Ti-magnetite crystals formed during quenching indicate rapid crystallization from a transient melt under conditions of strong undercooling and chemical disequilibrium.

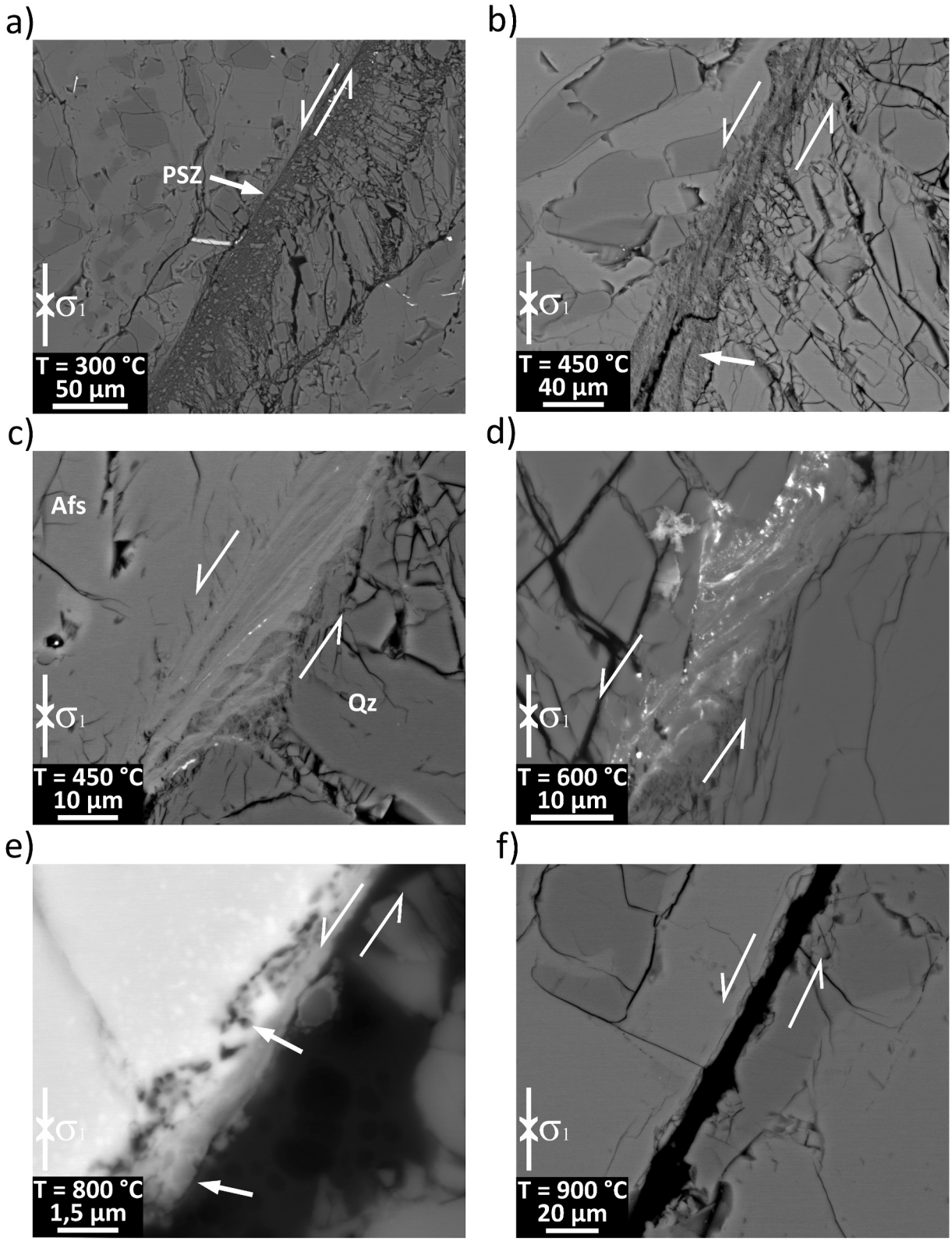

Figure 12.

grains of different composition (Figure 12e). Furthermore, we note that surface roughness of the saw-cut surfaces almost vanishes and flattens extremely.

3.2.2. Deformed Basalt

Up to 500°C, failure of the Rodderberg basalt samples occurs predominantly by the formation of a single main fracture inclined at approximately 30° to the deformation axis, accompanied by several sub-parallel cracks that propagate along pre-existing but re-sealed microcracks (Figure A3a). These fractures exhibit an almost purely extensional character, with negligible evidence of shear displacement. Opposite sides of cracked grains can be readily matched, and the fractures lack signs of grain comminution, gouge formation, or any surrounding damage zone. Localized zones of more intense damage occur only where fractures intersect, producing comminuted minerals or fragmented rock clasts (Figure 13a). In some cases, conjugate cracks intersect to form wedge-split failures, leading to axial splitting, spalling, and edge breakouts. However, compared to the felsite samples deformed within the same temperature range, the overall abundance of microcracks and the extent of the damage zones surrounding major fractures are significantly smaller, typically not exceeding ∼100 μm in thickness. In the sample tested at 20°C, occasional opening of pre-existing microcracks (<5 μm wide) is observed; these propagate preferentially along grain boundaries and can extend up to ∼2 mm in length.

At 700°C, and independent of water content, deformation in the basalt samples is accommodated by slightly non-planar, undulating shear fractures along which strain is strongly localized. These mixed-mode structures exhibit alternating dilatational and contractional segments (Figure A3b), characterized by intense grain comminution and frictional sliding that generate gouge layers less than 50 μm thick. Dilatational zones, >500 μm wide, contain angular, weakly rotated fragments, whereas slip in contractional segments is concentrated within ultra-fine shear bands (∼10–20 μm wide; Figures 13b and 13c) composed of sub-rounded grains (<3 μm) embedded in a fine-grained (submicron sized), non-porous matrix with a composition unassignable to any primary mineral phase.

At 900°C, no distinct shear zone developed; instead, the deformed basalt sample exhibited bulging (Figure A3c). Strain was accommodated through the formation and opening of distributed microcracks, locally leading to compaction bands in areas of slightly elevated initial interparticle porosity (Figure 13d). Intracrystalline deformation of the larger phenocrysts as well as partial melting was not observed.

At 1100°C, deformation of the Rodderberg basalt is dominated by partial to extensive melting, leading to a fundamental transformation of the groundmass microstructure (Figures 13e and 13f). The original hyalopilitic fabric, composed of plagioclase and clinopyroxene laths with interstitial nepheline and albite, has largely melted to form a non-porous glass (Figures 13e and 13f). This glass differs chemically from the starting material, showing enrichment in SiO_2, Al_2O_3, and K_2O, and depletion in MgO and CaO, consistent with preferential melting of alkali-rich interstitial phases and retention of Mg- and Ca-rich minerals such as olivine and clinopyroxene. Larger olivine phenocrysts, particularly at sample margins, remain intact and are enclosed by the newly formed glass. Within the melt, dendritic clinopyroxene crystals developed either on residual pyroxene grains or directly from the melt, forming elongated, lath-shaped morphologies up to ∼75 μm long. Even in regions that did not melt completely, the groundmass displays a distinctly more angular and heterogeneous texture than the original basalt, reflecting partial melting, recrystallization, and rapid quenching during high-temperature deformation.

Similar to felsite, the deformed basalt split-cylinder samples show almost no barreling, but predominantly pure shear along the predefined fault plane. Deformation is mainly concentrated within a small damage zone containing fractured grains adjacent to the saw-cut fault. At temperatures <700°C a thin gouge layer (<30 μm) evolved (Figure 14a–14c), where a high amount of gouge correlates with strong strain hardening. At these temperatures, the fault surface is rough with an increasing amount of slickenlines at higher temperature, but less

Figure 12. Backscattered electron (BSE) images showing deformation structures of saw-cut samples of felsite at different temperatures. Up to 300°C, shear along the saw-cut surface is accommodated by cataclastic flow (a) with clear grain size reduction toward the principle slip zone (PSZ). At 450°C, intensive grain comminution is leading to the formation of ultrafine, sub-micron-sized grains (white arrow in b). Partially, melt occurs at narrow contact surfaces (c), forming flow structures consisting of a low-porous amorphous layer with varying chemical composition. As temperature increases, the amount of flow textures at contact surfaces increases, while the amount of cataclastic gouge decreases (d). At the highest applied temperatures of 800°C and 900°C, cataclasis is at its minimum and rarely observed (e and f) No damage zone developed in the vicinity of the saw-cut surfaces and shear was accommodated along a μm-thick layer of amorphous material exhibiting vesicles and containing spherical, sub-rounded grains (white arrows in e).

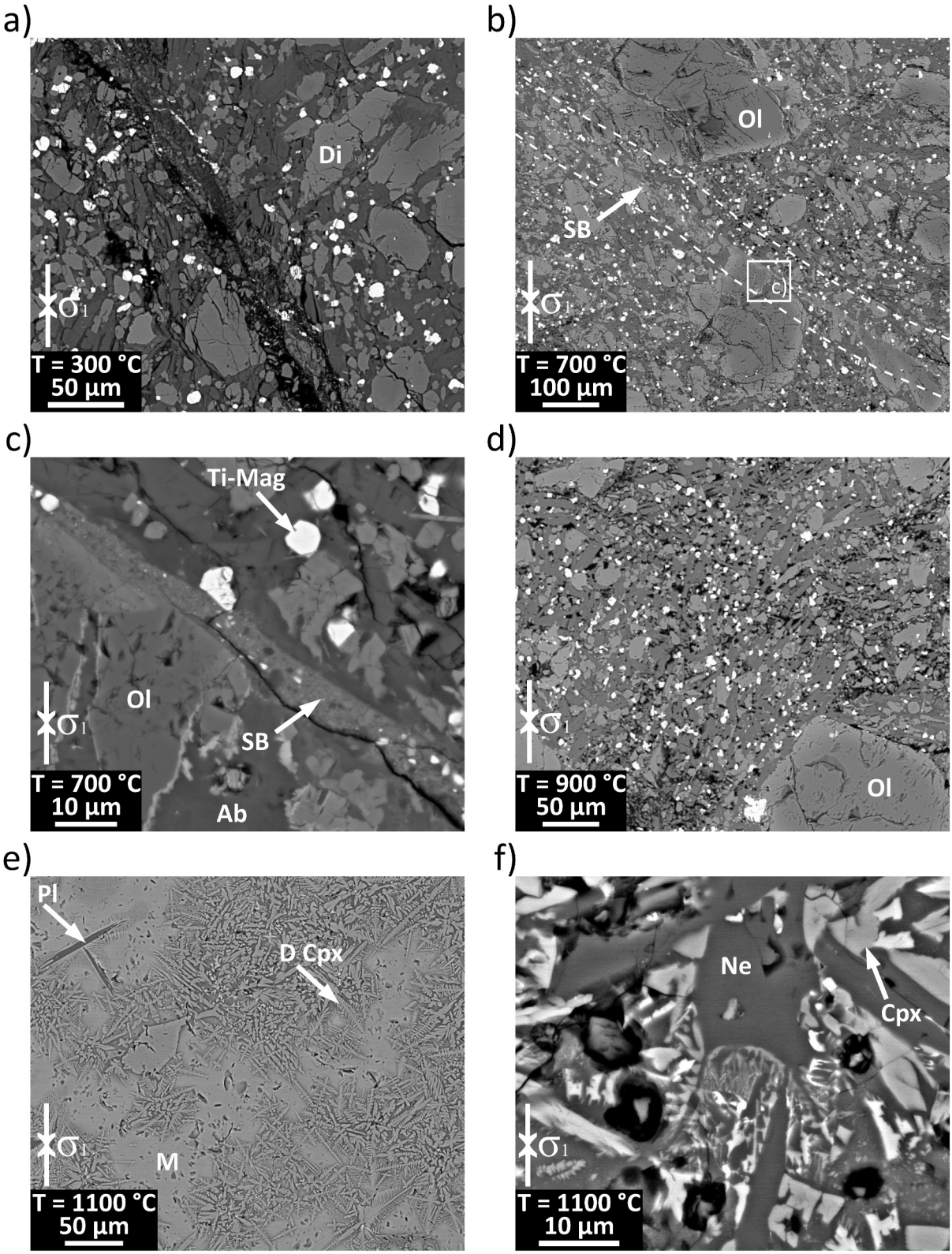

Figure 13.

deformation-induced powder production, in particular at $T \geq 500°C$. Microfractures are rare at the highest applied temperature of 700°C, associated with a relatively flat fault surface (Figures 14d and 14e) and often strain weakening (Figure 6d). TEM and SEM investigations reveal that during deformation under 700°C, partial melt formed within samples that show the lowest strength (Figure 6f), for example, sample BAS14, deformed at $P = 30$ MPa (Figure 14f) and sample BAS04 ($P = 50$ MPa).

4. Discussion

4.1. Triaxial Compressive Strength

Compressive strength obtained at 50 MPa pressure (sample fels_s02) fits the results obtained by Eggertsson (2019) as shown in the appendix (Figure A4). Eggertsson (2019) investigated the impact of pressure on peak strength of felsite rocks from Krafla at room temperature in experiments performed at a strain rate of 1×10^{-5} s^{-1} and confining pressures between 0.1 and 30 MPa. The author measured a non-linear increase of peak strength with pressure, which can be described by a Hoek-Brown failure criterion, expected to be induced by compaction of the porous rock. Fitting the data in small pressure intervals to a linear Mohr-Coulomb failure criterion results in decreasing internal friction coefficients with increasing pressure (Figure A4). In the pressure interval of 30–50 MPa, the internal friction coefficient is ≈0.62, which is close to the friction coefficient of $\mu = 0.69$ and the frictional resistance of $\mu_r = 0.68$ determined from the intersection point of saw-cut samples at room temperature (Table 3). Interestingly, the felsite strength data are quite similar to the triaxial strength data of Darley Dale sandstone (Murrell, 1965 in Sheorey, 1997), which is composed of 75% quartz, 15% feldspar and 10% miscellaneous with a porosity of 21% and permeability of about 5×10^{-14} m^2 (Murrell, 1965). The similarity of pressure-dependent strength suggests similar acting deformation mechanisms, likely due to the comparable composition but different origin of the two rock types. At $T = 100°C$ and $P = 50$ MPa the triaxial strength of porous Flechtinger sandstone (64 vol% quartz, 13% feldspar, 10% clay, 9% porosity) is about 300 MPa (Rybacki et al., 2015), quite similar to the strength of felsite with comparable porosity.

Concerning the influence of temperature on peak strength at 50 MPa pressure and laboratory strain rate ($\approx 5 \times 10^{-5} - 5 \times 10^{-4}$ s^{-1}), it is evident from Figure 4 that "dry" felsite reveals a relatively constant triaxial strength up to about 900°C above which the strength decreases considerably with temperature. The low temperature sensitivity of felsite up to 900°C, the shape of stress strain curves with mostly moderate strain weakening up to high strain after peak stress (Figure 3a), and the microstructural observations of deformed samples with abundant axial microcracks, the development of localized brittle fault zones (Figure 11; Figure A2) suggests high ductility with predominantly brittle deformation mechanisms, dominated by formation and coalescence of microcracks and pore collapse resulting in localized cataclastic flow. The variability of peak strength at given temperature may be explained by local variations of porosity and mineral composition. Interestingly, at 900°C the peak strength is maintained, but the sample showed strong strain weakening (Figure 3a) with first occurrence of melt, evidenced by the occurrence of brownish patches in plane-polarized images (Figure A2e and A2f) that correspond to the onset of Cpx melting. The latter was likely facilitated through pronounced grain comminution that resulted from highly localized deformation. The presence of fluids in the wet sample deformed at 900°C resulted in enhanced melt production relative to its dry counterpart, leading to considerably lower strength and distributed deformation (Figure 3; Figure A2). At a temperature of 1000°C and above, the strength decreases more and more with increasing partial melt content and the contribution of brittle microfracturing is subordinate with concurrent porosity reduction (Figure 11). We conclude that dry intact felsite samples exhibit pronounced post peak deformation with strain weakening under laboratory strain rates. Below about 900°C strength is hardly influenced by temperature, but decreases at higher temperature and/or water content induced by a change from cataclastic flow to melt-assisted ductile creep.

In contrast, the low-porosity basalt behaves much more brittle at low temperature, that is, below 700°C (Figure 3b), and strength decreases almost continuously with increasing temperature. The strength of basalt is

Figure 13. Backscattered electron (BSE) images showing the temperature-dependent microstructural evolution of Rodderberg basalt during deformation. Up to 500°C, deformation is accommodated by single extensional fractures that locally form cataclastic zones where they intersect (a). At 700°C, strain localizes within non-planar shear bands (SB) in contractional zones composed of fine-grained amorphous material (b, c). At 900°C, deformation occurs through distributed microcracking and pore collapse (d). At 1100°C, partial melting produces a dendritic network of clinopyroxene (D Cpx) and plagioclase (Pl) within a melt matrix (M), with newly formed dendritic clinopyroxene crystals and melt-induced modification of crystal shapes (f).

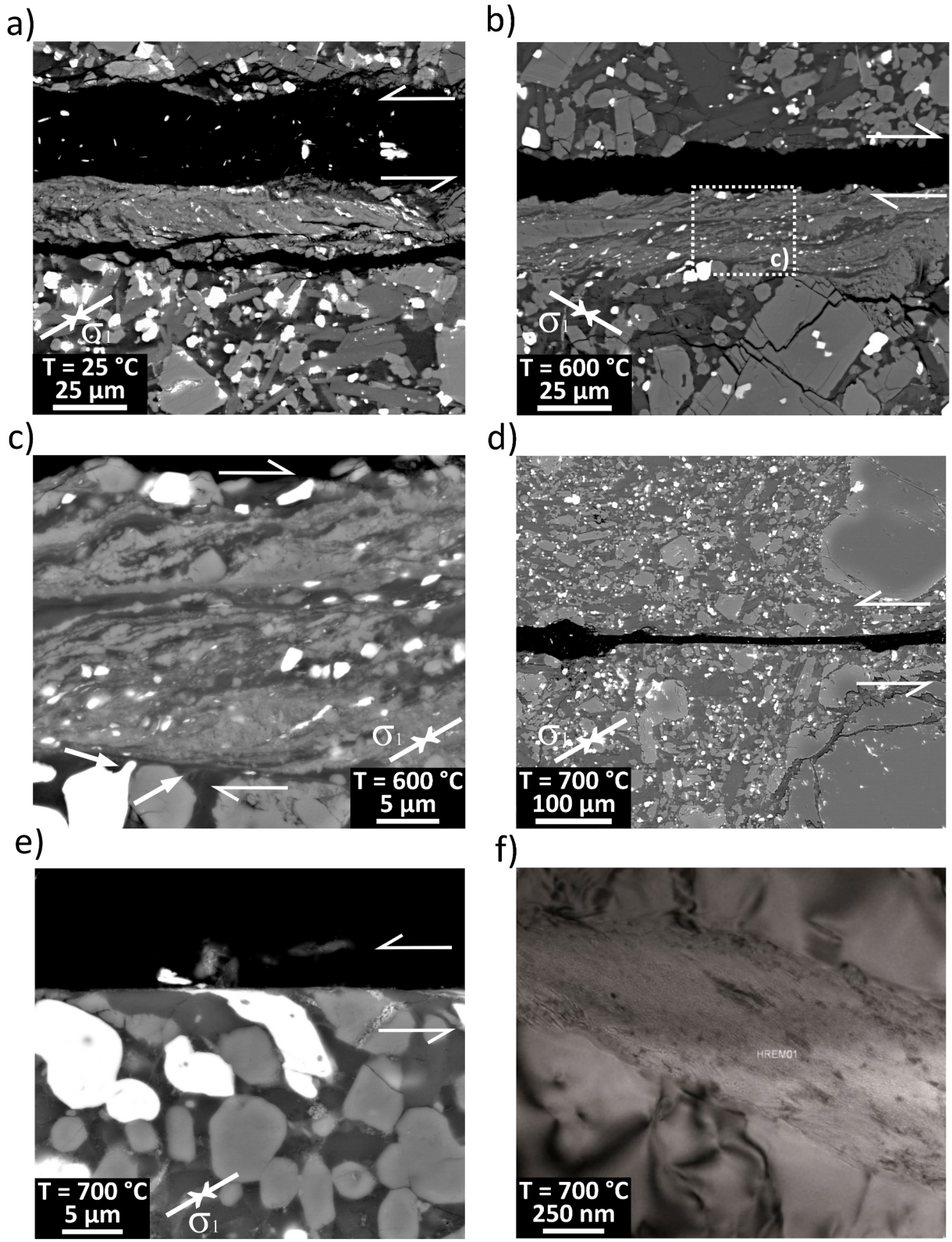

Figure 14. Microphotographs of sheared saw-cut basalt samples. (a) BSE image of the damage zone adjacent to the fault of sample BAS08 ($T = 25°C$, $P = 50$ MPa) with fine-grained gouge in the center produced by cataclastic flow. (b) Gouge evolution in sample BAS07 ($T = 600°C$, $P = 50$ MPa) with magnification shown in (c). At high temperature, minor microfracturing (d) and a smooth fault surface (e) is evident in sample BAS09 ($T = 700°C$, $P = 50$ MPa, left-lateral movement). (f) High resolution transmission electron microscope micrograph of a melt pocket in sample BAS14 ($T = 700°C$, $P = 30$ MPa). Note different scales.

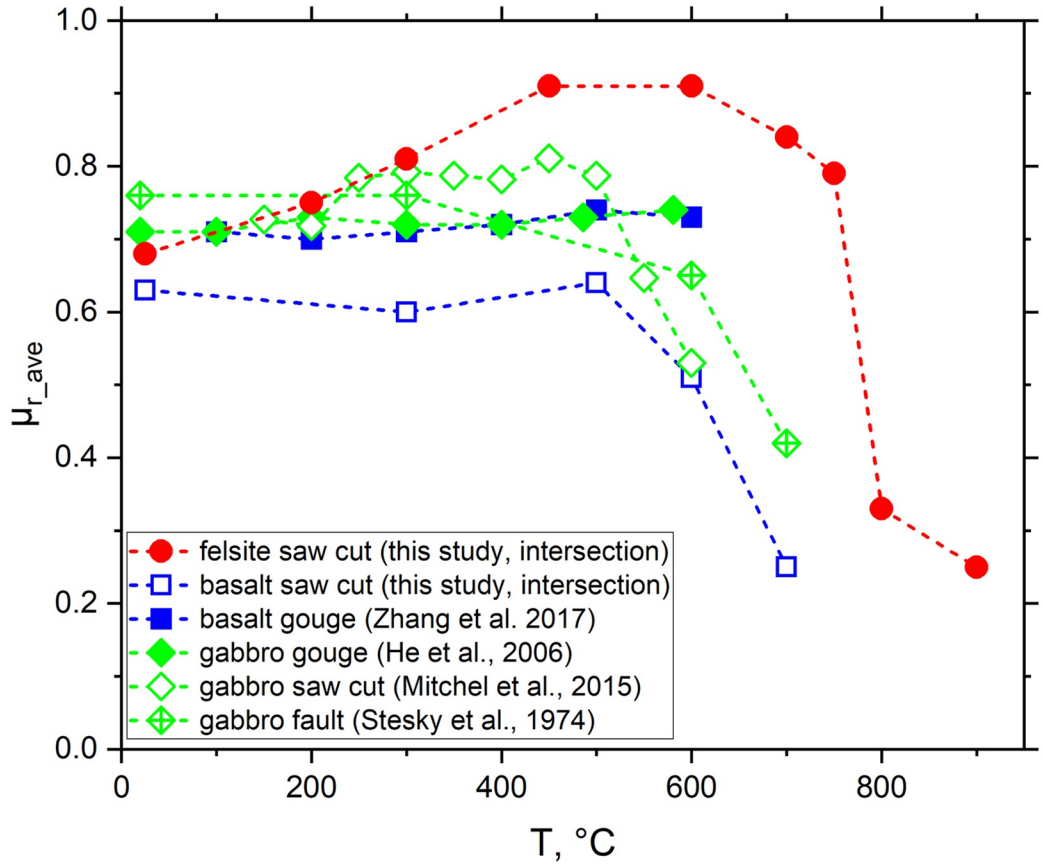

Figure 15. Comparison of high temperature frictional resistance of felsite and basalt saw cut samples with data measured for basalt gouge (P = 50 MPa, Zhang et al., 2017), gabbro gouge (P = 200 MPa, He et al., 2006), gabbro saw cut (P = 5 MPa, Mitchell et al., 2015), and gabbro fault (P = 100–600 MPa, Stesky et al., 1974).

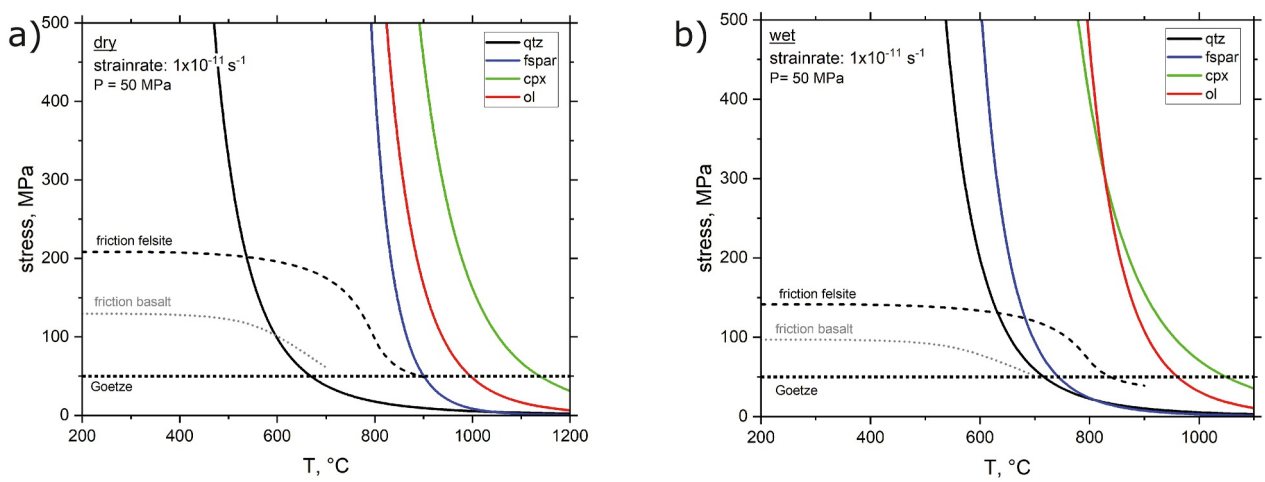

Figure 16. Creep stress for dislocation creep of quartz, feldspar, clinopyroxene and olivine aggregates at in situ strain rate of 1×10^{-11} s^{-1} at elevated temperatures under dry (a) and wet (b) conditions. Short dotted line at 50 MPa represents the Goetze criterion for the onset of the brittle plastic transition. Frictional strength of felsite and basalt are approximated from our measurements on sawcut samples. Flow laws for olivine are provided by Hirth and Kohlstedt (2003), for clinopyroxene by Dimanov and Dresen (2005), for feldspar by Rybacki et al. (2006), and for dry and wet quartz by Jaoul et al. (1984) and Rutter and Brodie (2004), respectively.

considerably higher compared to felsite at $T \leq 700°C$, where it shows minor inelastic deformation before (first) failure (Figure 3b) in conjunction with localized cracking and limited damage zones compared to felsite. In general, a strong temperature sensitivity of compressive strength indicates that non-brittle deformation processes are active. Yet, we do not see microstructural evidence for plastic deformation mechanisms to be active in basalt samples. A similarly strong temperature dependence of deformed basalt was observed by Violay et al. (2012) (see Figure 4 in Violay et al., 2012). Possibly, stress corrosion-induced brittle creep (e.g., Heap et al., 2011) may play a role here, even under nominal "dry" conditions. Alternatively, local contact forces induced by different thermal expansion coefficients of the constitutive minerals may induce damage in response to heating. At $T = 700°C$ gouge production is more prominent and shear bands develop (Figure 13). At this temperature, the wet sample deforms more ductile and homogeneously at considerably lower strength than its dry counterpart (Figure 3b), likely attributed to a reduced effective pressure of the undrained experiments. Above 700°C the dry basalt samples show ductile behavior with pronounced inelastic deformation and a strong reduction of strength, which is associated with distributed microcracking accompanied by pore collapse at 900°C and by partial melting with minor fracturing at 1100°C (Figure 13).

Our data of deformed basalt may be compared to high temperature strength data obtained at 100 MPa effective pressure and a strain rate of 1×10^{-5} s^{-1} for wet Languedoc-Roussillon basalt (Violay et al., 2012). Evidently, except at $T = 700°C$, the wet basalt (≈40% feldspar, 30% pyroxene, 10% feldspathoids, 10% titanomagnetite, few olivines, 2%–3% porosity) is considerably stronger than the dry basalt measured in this study (Figure 4). This difference is likely explained by the higher confining pressure compared to our measurements, which enhances strength in the (semi-) brittle regime. The wet basalt also shows a strong reduction of triaxial strength with increasing temperature. The authors observed localized brittle deformation behavior up to 900°C, but ductile (non-localized) behavior at 300 MPa pressure, revealing that high confinement suppresses dilatant microcracking.

4.2. Frictional Strength

For both investigated rock types, the average frictional resistance is higher than the friction coefficient because of non-zero cohesion (Figure A1). It is also higher if determined from the intersection point compared to yield point stress (Figures 8 and 10), where the latter represents minimum (initial) friction conditions. Yield point friction values are quite variable, but on average well below 0.5, which is in line with low temperature initial friction data collected by Byerlee (1978). In the following we discuss the values obtained at the intersection point, which is closer to the maximum friction values that are obtained if no hardening occurs, for example, data that are usually described by friction laws for rocks (Byerlee, 1978).

The observation that the frictional strength of felsite saw-cut samples decreases with increasing confining pressure at temperatures ≥800°C (Figures 5g and 5h) is interpreted as being induced by an increasing amount of partial melt due to ongoing deformation with grain comminution and lowering of the solidus temperature in (wet) granitic systems.

Our basalt saw-cut samples show the occurrence of gouge at low temperature, associated with strain hardening. At low to intermediate temperature, the measured friction coefficient of felsite is between ≈0.7 and 1.0 ($T \leq 750°C$, Table 3, Figure 8a) and of basalt between about 0.4 and 0.5 ($T \leq 500°C$, Table 4, Figure 10a), which is in line with other maximum frictional data on silicate rocks measured at low temperature (Byerlee, 1978; Ikari et al., 2011). The mean frictional resistance at the intersection point $\mu_{r\_ip\_ave}$ is in a similar range, but drops down to values ≤0.33 for felsite at $T \geq 800°C$ and to $\mu_{r\_ip\_ave} = 0.25$ for basalt at $T = 700°C$ (Figures 8b and 10b). This remarkable reduction is induced by the presence of melt in sheared felsite and basalt samples. Compared to the deformed intact samples, the melt-induced strength reduction is about 200°C lower, which is presumably caused by the presence of absorbed fluids on the saw-cut surfaces during assembling.

For comparison, high temperature frictional resistance data from other rocks (basalt and gabbro) are shown in Figure 15. Evidently, the frictional resistance also starts to decrease with temperature above about $T = 500°C$ for gabbro saw-cut samples (Mitchell et al., 2015) and faulted gabbro samples (Stesky et al., 1974). For basalt and gabbro gouge no reduction was measured up to 600°C (He et al., 2006; Zhang et al., 2017), revealing that fault maturity affects the onset of weakening. Note that besides fault roughness other factors such as fault composition,

water content and sliding rate affect the frictional behavior (e.g., Blanpied et al., 1995; Di Toro et al., 2011; Hu & Sun, 2020; Scholz, 2019; Stesky, 1978; Violay et al., 2019).

4.3. Application for Supercritical EGS

One major concern for utilizing geothermal reservoirs at very high temperature, i.e., beyond the BPT, is the potential risk of permeability being too low for efficient use (e.g., Stimac et al., 2015). Despite the assumption that plastic flow at high temperature may result in low permeability (e.g., Acosta et al., 2020; Fournier, 1999; Stimac et al., 2015), it is still an open question if high permeability can be maintained at high temperature (e.g., Reinsch et al., 2017). Experimental and theoretical studies suggest that across the BPT the permeability reduction is smooth and sufficient permeability may be maintained because the formation of tensile fracs in response to thermal or hydraulic stimulations can outlast the live time of a geothermal power plant (Goto et al., 2021; Kushnir et al., 2017; Lavallée et al., 2020; Parisio et al., 2020, 2021; Siratovich et al., 2015; Violay et al., 2017; Watanabe, Egawa, et al., 2017; Watanabe, Numakura, et al., 2017; Watanabe et al., 2020, 2020; Yapparova et al., 2023).

At Krafla, the existence of a permeable shallow layer may be explained by the observation that cooling-induced cracking of basalt can initiate just 100°C below the solidus (Lamur et al., 2018). In case of the IDDP-1 borehole, the felsite adjacent to the magma chamber is expected to be "ductile" (plastic) close to the solidus and brittle only a few tens of meters above the magma chamber where temperatures are less than about 500°C (Eichelberger, 2020). Our data show that at 50 MPa pressure the measured frictional strength of felsite and basalt is always lower than the bulk (matrix) peak strength of these rock types (Tables 1–4, Figures 4–6), revealing that thermally induced fractures will be activated before bulk deformation occurs. Note however, that the deformation may be partitioned into partial fault reactivation and partial bulk deformation, depending on confinement and temperature (Meyer et al., 2019; Niu et al., 2024), in particular for felsite that shows ductile (non-localized) behavior of intact samples.

The measurements presented in this study indicate that under laboratory conditions dense basalt deforms brittle (localized) at temperatures up to about 700°C and 50 MPa pressure with a strongly temperature dependent strength. In contrast, porous felsite reveals low temperature sensitivity of strength in the same temperature interval and shows ductile (non-localized) deformation up to about 900°C. The difference in temperature dependence on compressive strength between both rock types is likely attributed to compaction of the porous felsite. The onset of partial melting and pore collapse starts at about 900°–1000°C for felsite and at 900°C–1100°C for basalt. Therefore, our observations on intact felsite samples suggest that fracture closure due to the onset of plastic deformation of rocks is unlikely, even close to the magma chamber at the Krafla test site (at $T \approx 900$°C), at least at the (fast) strain rates imposed in the laboratory. Note, however, that this conclusion is only valid at a confinement of 50 MPa, which was used in this study. A rough estimation of the pressure required to initiate the BDT may be based on equating the fracture strength of intact samples with the differential stress necessary to cause sliding along an optimally oriented, pre-existing fault (Byerlee, 1968). The strong pressure dependence of intact felsite (Figure A4) suggests that at pressures far above 50 MPa the BDT may occur, but due to the lack of strength data at different pressures and high temperature, this remains speculative and is probably not important for the KMT project. Note, however, that recent deformation experiments on granite at high temperatures showed that permeability is considerably enhanced if deformed in the semi-brittle deformation regime with strain hardening (Meyer et al., 2024), which contradicts the assumption that the BDT reduces fluid flow at large depth.

At geological strain rates the situation may be different since both the BDT and the BPT are likely to depend on strain rate. Assuming that semi-brittle flow strength can be approximated by a power-law creep equation, estimated "brittle-ductile" transition temperature at geological strain rates of 10^{-14} s^{-1} is ≈550°C for basalt (Violay et al., 2012). However, so far, no constitutive equation for the strength of rocks in the semi-brittle regime exists (Brantut, 2025; Rybacki et al., 2021). If we consider the transition from brittle or semi-brittle to plastic flow (BPT), strain rate plays an important role because the plastic creep strength is related to strain rate by a power law relationship (e.g., Evans & Kohlstedt, 1995). The BPT of silica-rich rocks such as granite is expected to be about 360–400°C (Foumier, 1991, 1999). In terms of common minerals of the continental crust, the onset of plasticity (BPT) at natural strain rate is about 300°C for quartz, 500°C for feldspar and 700°C for olivine and pyroxene, respectively (e.g., Bürgmann & Dresen, 2008; Passchier & Trouw, 1996), indicating that felsic (qtz-fspar-rich) rocks likely have a lower BPT temperature than (ultra-)mafic (px-ol-rich) rocks. As a rule of thumb, the BDT can

be estimated from the empirical Goetze criterion, which suggests that the onset of plasticity occurs if the rock strength is lower than the confining pressure so that dilatant behavior due to sliding of microcracks is unlikely (Kohlstedt et al., 1995). In our tests, the peak strength was always higher than the confining pressure except at $T = 1100$°C (Figure 4), suggesting that the BPT was not reached under the selected laboratory strain rate (5×10^{-5} s^{-1}), in agreement with the microstructural observations.

To estimate the conditions at lower strain rates, we use existing flow laws for plastic creep of minerals to calculate creep strength at a relatively fast "geological" strain rate of 1×10^{-11} s^{-1}, representative for few percent strain within an assumed live time of a supercritical geothermal systems of about 50 years. Here, we calculate creep strength from flow laws of monomineralic rocks as endmember conditions of polyphase rocks. We use existing flow laws for quartz feldspar, pyroxene, and olivine to simulate the behavior of quartz-feldspar-rich rocks like felsite and of feldspar-pyroxene-olivine-rich rocks like basalt. Comparison of the creep strength with the Goetze criterion (here 50 MPa confinement) suggest the onset of the BPT at temperatures between 670° and 900°C (average 790 ± 120°C) for dry felsite and between 900 and 1140°C (average 1020 ± 120°C) for dry basalt (intersection of solid lines with the 50 MPa Goetze criterion line in Figure 16a). Under wet conditions the onset is predicted to be in the range of 720°–740°C (mean 730 ± 10°C) for felsite and between 740° and 1050°C (mean 900 ± 160°C) for basalt (Figure 16b). Using instead an order of magnitude lower strain rate (10^{-12} s^{-1}) yields about 60°C lower transition temperatures. The presence of olivine in basalt will not change theses estimates since the extrapolated strength of olivine is between the strength of feldspar and pyroxene (Figure 16). Alternatively, if we neglect semi-brittle deformation, the BPT may be also estimated from the intersection between frictional strength and extrapolated flow laws. For simplicity, we approximated the frictional behavior of felsite by a fixed cohesion of 10 MPa and a friction coefficient of ≈0.8 at $T \leq 750$°C, 0.3 at $T = 800$°C and $\mu = 0.2$ at $T = 900$°C (cf. Table 3). For basalt we used $\mu \approx 0.5$ at $T \leq 500$°C, 0.4 at $T = 600$°C and $\mu = 0.2$ at $T = 700$°C with a constant cohesion of about 15 MPa (cf. Table 4). For a thrust fault regime, the differential stress for friction can then be calculated from the equation (Jaeger & Cook, 1969) $\Delta\sigma_{TF} = [2c \cos\phi + 2S_V(1 - \lambda) \sin\phi]/(1 - \sin\phi)$ with $\mu = \tan\phi, \lambda = P_0/S_V \approx 0.4$ for hydrostatic water pressure P_0 of 20 MPa and a vertical stress of $S_V \approx 50$ MPa at 2 km depth. For dry and wet felsite the BPT is then then estimated at $T \approx 720 \pm 180$°C (540–900°C) and $T \approx 660 \pm 30$°C (630–680°C), respectively (intersection of broken and solid lines in Figure 12), that is, about 70°C less than the corresponding BPT temperatures estimated from the comparison to the Goetze criterion. For basalt, no friction data are available at very high temperature (cf. Figure 16). These simple estimations indicate a brittle-plastic transition temperature, T_{BPT}, in the order of 720–790°C for dry felsite and 660°–730°C for wet felsite, albeit with large uncertainty, suggesting that fracture closure close to the magma chamber at Krafla (at $T \approx 900$°C) can be expected at low (geological) strain rate. For basalt, T_{BPT} is considerably (170–230°C) higher than for felsite, indicating that at the IDDP-1 borehole, where there is a large temperature gradient close to the magma chamber, plastic flow-induced fracture closure of basalt is unlikely. Note, that the brittle-ductile transition temperature, T_{BDT}, at a strain rate of 1×10^{-14} s^{-1} is estimated to be about 550 ± 100°C for wet basalt (Violay et al., 2012), meaning that non-localized deformation may occur close to the magma body under wet conditions and at geological strain rates. If the basalt contains glass, as indicated by cutting analysis of basalt found at low depth in well IDDP-1 (Mortensen et al., 2014), the estimated transition temperature is considerably lower (about 100°C, Violay et al., 2012). It should be also noted, that partial crack closure and permeability reduction may be also induced at low temperature under wet conditions due to stress corrosion-induced brittle creep (Heap, Baud, & Meredith, 2009; Heap, Baud, Meredith, Bell, & Main, 2009, 2011).

5. Conclusions

We performed a set of triaxial compression tests on intact felsite and basalt samples and shear deformation experiments on similar samples with a pre-defined favorably oriented saw-cut at pressures between 30 and 90 MPa, temperatures up to 1100°C and constant axial strain rates of about 5×10^{-5} s^{-1}. The data may help to assess the possibility to install a supercritical geothermal power plant within the KMT project. Prior to the onset of partial melting the mechanical data show poorly temperature-dependent stress-strain behavior of felsite and highly temperature-sensitive behavior of basalt. The felsite shows a gradual transition from moderate brittle to ductile behavior with increasing delocalization and pronounced post peak strain weakening at higher temperature, whereas the basalt deforms brittle with strongly localized fracture evolution and sharp stress drops after reaching the peak strength. Wet samples were softer than their dry counterparts. Peak strength of dry felsite and basalt

decreases strongly at temperatures above about 900 and 700°C, respectively, whereas frictional strength decreases at about 200°C lower temperatures ($T \geq 750$°C for felsite and $T \geq 500$°C for basalt).

From the data obtained at laboratory strain rate and the estimated temperature for the onset of the BPT at in situ strain rate we conclude that at the *P-T* conditions at the Krafla test site close to the magma chamber (50 MPa, ≈900°C), fracture closure and an associated drastic reduction of the formation permeability of the felsite aureole is unlikely on the short term, but more likely on the long term, which supports the reservoir behavior suggested by Eichelberger (2020).

Appendix A

The dependence of measured cohesion values for felsite and basalt up to 750°C is shown in Figure A1. Thin-section micrographs of deformed intact felsite (A2) and basalt (A3) showing the influence of increasing temperature on crack pattern and melt evolution. Peak differential stress of felsite determined at room temperature increases with increasing confining pressure (Figure A4). See main text for details.

Figure A2.

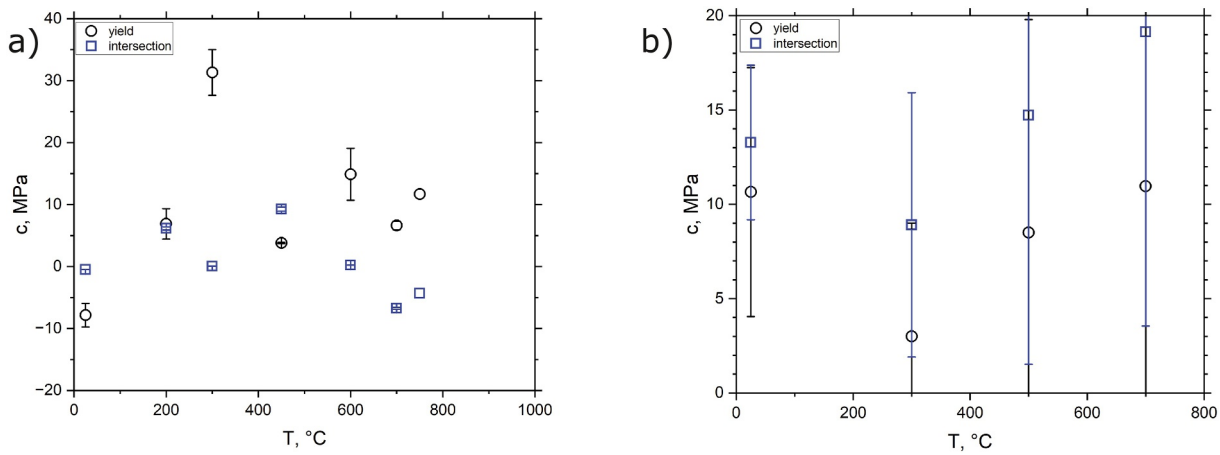

Figure A1. Variation of cohesion *c* with temperature for felsite (a) and basalt (b) saw-cut samples. Note that few negative values are physically unrealistic, resulting from the applied fitting procedure.

Figure A3.

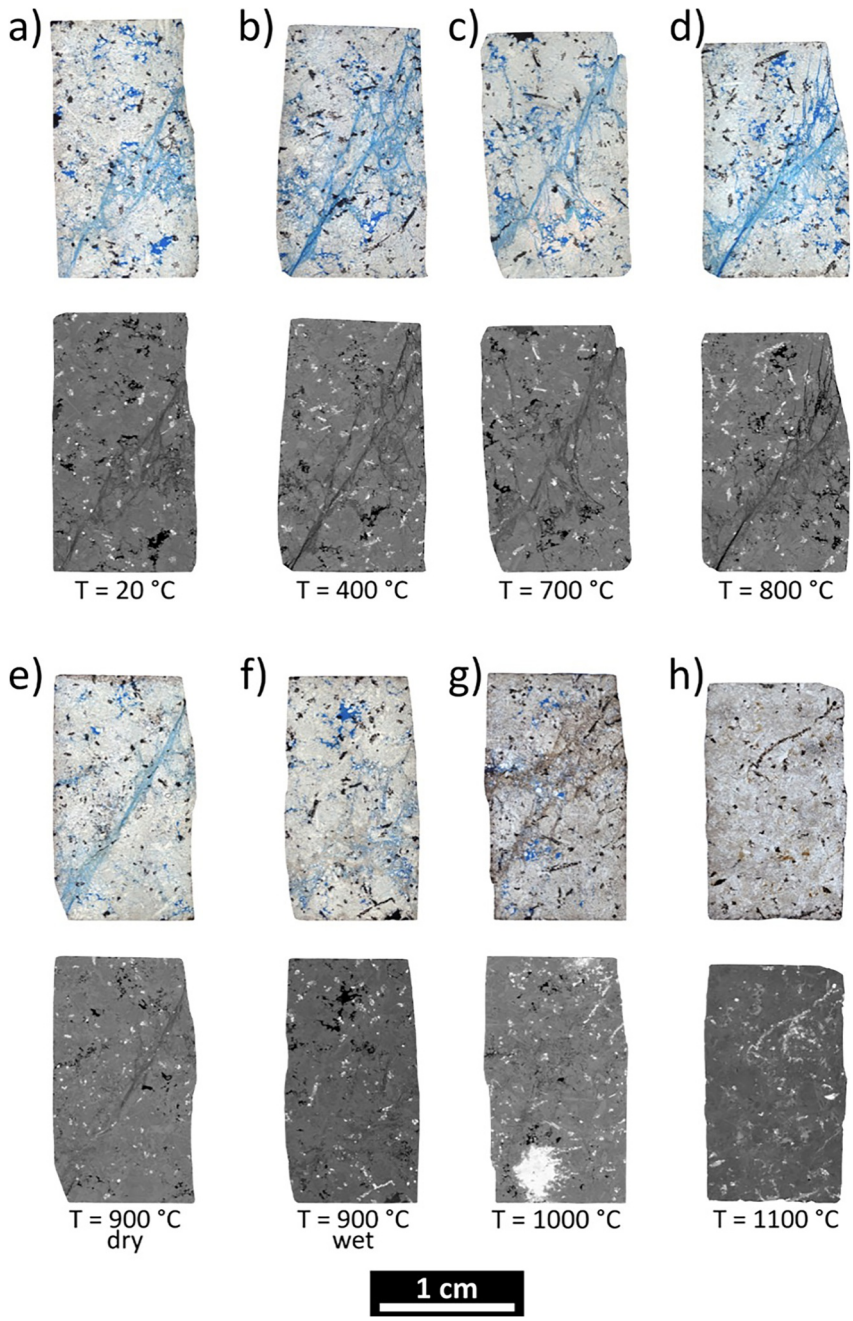

Figure A2. Microstructures of deformed felsite samples across increasing temperatures, shown in plane-polarized light (top) and BSE images (bottom). The sequence captures the transition from brittle cataclastic deformation (a–d) to ductile shearing (e), incipient melting (f–g), and fully melt-dominated flow (h), illustrating the progressive rheological evolution with temperature. A marked reduction in porosity is observed with increasing temperature, particularly above 900°C, as deformation becomes increasingly accommodated by viscous and melt-assisted processes.

Figure A4.

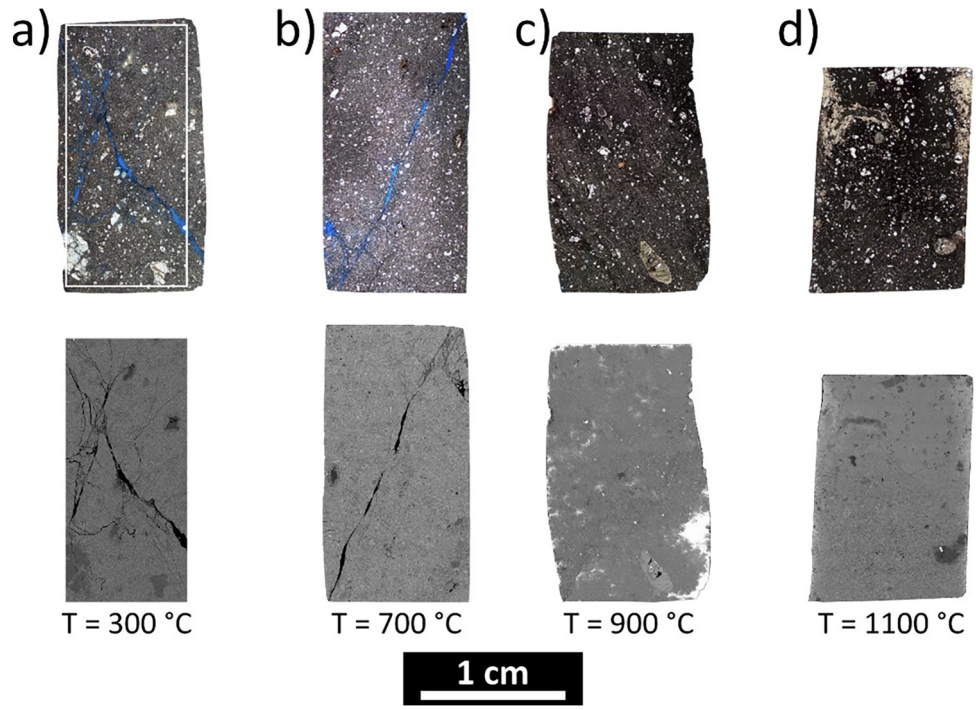

Figure A3. Microstructures of deformed basalt samples with increasing deformation temperature, shown in plane-polarized light (top) and backscattered electron (BSE) images (bottom). The sequence illustrates the transition from brittle, cataclastic deformation (a–b), through ductile flow (c), to fully melt-dominated flow (d). Note that in (a), only part of the thin section was imaged with the scanning-electron microscope (white rectangular), and in (d), approximately two-thirds of the sample deformed at 1100°C is shown, as it had to be cut free from the jacket.

Conflict of Interest

The authors declare no conflicts of interest relevant to this study.

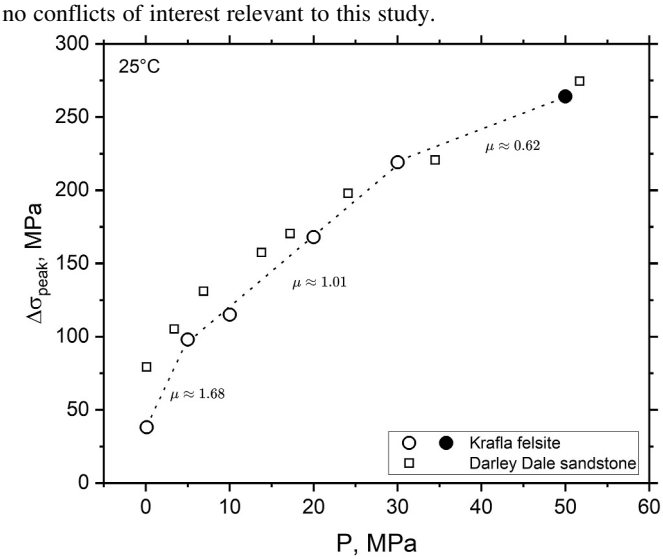

Figure A4. Increase of peak differential stress of felsite with confining pressure at 25°C temperature. Open circles represent data measured at a strain rate of 1×10^{-5} s^{-1} (Eggertsson, 2019) and solid circle at 5×10^{-5} s^{-1} (this work). Linear fitting of stresses in confining pressure intervals of 0.1–5 MPa, 5–30 MPa, and 40–50 MPa yields internal friction coefficients of 1.68, 1.01 and 0.62, respectively (cf., Equations 6 and 8). Measurements on Darley sandstone were done at a strain rate of 1×10^{-4}–1×10^{-5} s^{-1} (Murrell, 1965).

Availability Statement

The stress-strain data of all samples used in this paper are available at (Rybacki et al., 2026).

Acknowledgments
We like to thank Yan Lavallée and Nikolaus Froitzheim for providing the samples, Anja Schleicher for performing XRD analysis, Anja Schreiber for FIB sections preparation and Richard Wirth for TEM analysis. We are grateful to Michael Naumann for his help with the experiments and to Stefan Gehrmann for sample and thin section preparation. We also like to thank one anonymous reviewer and an associate editor for comments as well as the editor for handling of the manuscript. Open Access funding enabled and organized by Projekt DEAL.

References

Acosta, M., Gibert, B., & Violay, M. (2020). From brittle to ductile deformation in the continental crust: Mechanics of crystalline reservoirs and implications for hydrothermal circulation. In *Proceedings world geothermal Congress reykjavik*.

Árnason, K. (2020). New conceptual model for the magma-hydrothermal-tectonic System of Krafla, NE Iceland. *Geosciences*, *10*(1), 34. https://doi.org/10.3390/geosciences10010034

Asanuma, H., Muraoka, H., Noriyoshi, T., & Ito, H. (2012). The concept of the Japan Beyond-Brittle Project (JBBP) to develop EGS reservoirs in ductile zones. *Transactions - Geothermal Resources Council*, *36*, 359–364.

Baud, P., Wong, T.-f., & Zhu, W. (2014). Effects of porosity and crack density on the compressive strength of rocks. *International Journal of Rock Mechanics and Mining Sciences*, *67*, 202–211. https://doi.org/10.1016/j.ijrmms.2013.08.031

Blanpied, M. L., Lockner, D. A., & Byerlee, J. D. (1995). Frictional slip of granite at hydrothermal conditions. *Journal of Geophysical Research*, *100*(B7), 13045–13064. https://doi.org/10.1029/95jb00862

Brantut, N. (2025). Semi-brittle flow of rocks: Cracks, dislocations and strain hardening. *Proceedings of the Royal Society A: Mathematical, Physical and Engineering Sciences*, *481*(2307), 20240189. https://doi.org/10.1098/rspa.2024.0189

Bürgmann, R., & Dresen, G. (2008). Rheology of the lower crust and upper mantle: Evidence from rock mechanics, geodesy, and field observations. *Annual Review of Earth and Planetary Sciences*, *36*(1), 531–567. https://doi.org/10.1146/annurev.earth.36.031207.124326

Byerlee, J. (1968). Brittle-ductile transition in rocks. *Journal of Geophysical Research*, *73*(14), 4741–4750. https://doi.org/10.1029/jb073i014p04741

Byerlee, J. (1978). Friction of rocks. *Pure and Applied Geophysics*, *116*, 615–626.

Dimanov, A., & Dresen, G. (2005). Rheology of synthetic anorthite-diopside aggregates: Implications for ductile shear zones. *Journal of Geophysical Research*, *110*(B7), B07203. https://doi.org/10.1029/2004JB003431

Di Toro, G., Han, R., Hirose, T., De Paola, N., Nielsen, S., Mizoguchi, K., et al. (2011). Fault lubrication during earthquakes. *Nature*, *471*(7339), 494–498. https://doi.org/10.1038/nature09838

Eggertsson, G. H. (2019). *Constraining mechanical and permeability properties of the Krafla geothermal reservoir, North-East Iceland. 119*. PhD-Thesis. University of Liverpool.

Eggertsson, G. H., Lavallée, Y., Kendrick, J. E., & Markússon, S. H. (2020). Improving fluid flow in geothermal reservoirs by thermal and mechanical stimulation: The case of Krafla volcano, Iceland. *Journal of Volcanology and Geothermal Research*, *391*, 106351. https://doi.org/10.1016/j.jvolgeores.2018.04.008

Eichelberger, J. (2020). Distribution and transport of thermal energy within magma–hydrothermal systems. *Geosciences*, *10*(6), 212. https://doi.org/10.3390/geosciences10060212

Eichelberger, J., Ingolfsson, H., Carrigan, C. R., Lavallée, Y., Tester, J., & Markússon, S. H. (2018). Krafla magma testbed: Understanding and using the magma-hydrothermal connection. *GRC Transactions*, *42*.

Elders, W. A., Friðleifsson, G. Ó., & Pálsson, B. (2014). Iceland Deep Drilling Project: The first well, IDDP-1, drilled into magma. *Geothermics*, *49*, 1. https://doi.org/10.1016/j.geothermics.2013.08.012

Elders, W. A., Friðleifsson, G. Ó., Zierenberg, R. A., Pope, E. C., Mortensen, A. K., Guðmundsson, Á., et al. (2011). Origin of a rhyolite that intruded a geothermal well while drilling at the Krafla volcano, Iceland. *Geology*, *39*(3), 231–234. https://doi.org/10.1130/g31393.1

Evans, B., & Kohlstedt, D. L. (1995). Rheology of rocks. In T. J. Ahrens (Ed.), *Rock physics and phase relations: A handbook of physical constants, Ref. Shelf* (pp. 148–165). AGU.

Foumier, R. O. (1991). The transition from hydrostatic to greater than hydrostatic fluid pressure in presently active continental hydrothermal systems in crystalline rock. *Geophysical Research Letters*, *18*(5), 955–958. https://doi.org/10.1029/91gl00966

Fournier, R. O. (1999). Hydrothermal processes related to movement of fluid from plastic into brittle rock in the magmatic-epithermal environment. *Economic Geology*, *94*(8), 1193–1211. https://doi.org/10.2113/gsecongeo.94.8.1193

Friðleifsson, G. Ó., Elders, W., Zierenberg, R., Stefánsson, A., Fowler, A., Harðarson, B., et al. (2017). The Iceland Deep Drilling Project 4.5 km deep well, IDDP-2, in the seawater recharged Reykjanes geothermal field in SW Iceland has successfully reached its supercritical target. *Scientific Drilling*, *23*, 1–12. https://doi.org/10.5194/sd-23-1-2017

Friðleifsson, G. Ó., Elders, W. A., & Albertsson, A. (2014). The concept of the Iceland deep drilling project. *Geothermics*, *49*, 2–8. https://doi.org/10.1016/j.geothermics.2013.03.004

Frost, H., & Ashby, M. (1982). Deformation-mechanism maps. In *The plasticity and creep of metals and ceramics*. Pergamon Press.

Goto, R., Watanabe, N., Sakaguchi, K., Miura, T., Chen, Y., Ishibashi, T., et al. (2021). Creating cloud-fracture network by flow-induced microfracturing in superhot geothermal environments. *Rock Mechanics and Rock Engineering*, *54*(6), 2959–2974. https://doi.org/10.1007/s00603-021-02416-z

Hayba, D. O., & Ingebritsen, S. E. (1997). Multiphase groundwater flow near cooling plutons. *Journal of Geophysical Research*, *102*(B6), 12235–12252. https://doi.org/10.1029/97jb00552

He, C., Yao, W., Wang, Z., & Zhou, Y. (2006). Strength and stability of frictional sliding of gabbro gouge at elevated temperatures. *Tectonophysics*, *427*(1–4), 217–229. https://doi.org/10.1016/j.tecto.2006.05.023

Heap, M. J., Baud, P., & Meredith, P. G. (2009). Influence of temperature on brittle creep in sandstones. *Geophysical Research Letters*, *36*(19), L19305. https://doi.org/10.1029/2009GL039373

Heap, M. J., Baud, P., Meredith, P. G., Bell, A. F., & Main, I. G. (2009). Time-dependent brittle creep in Darley Dale sandstone. *Journal of Geophysical Research*, *114*(B7). https://doi.org/10.1029/2008JB006212

Heap, M. J., Baud, P., Meredith, P. G., Vinciguerra, S., Bell, A. F., & Main, I. G. (2011). Brittle creep in basalt and its application to time-dependent volcano deformation. *Earth and Planetary Science Letters*, *307*(1–2), 71–82. https://doi.org/10.1016/j.epsl.2011.04.035

Hirth, G., & Kohlstedt, D. L. (2003). Rheology of the upper mantle and the mantle wedge: A view from the experimentalists. In J. Eiler (Ed.), *The subduction factory* (pp. 83–105). AGU.

Hu, J., & Sun, Q. (2020). The effect of high temperature and pressure on rock friction coefficient: A review. *International Journal of Earth Sciences*, *109*(2), 409–419. https://doi.org/10.1007/s00531-019-01810-x

Ikari, M. J., Marone, C., & Saffer, D. M. (2011). On the relation between fault strength and frictional stability. *Geology*, *39*(1), 83–86. https://doi.org/10.1130/g31416.1

Jaeger, J., & Cook, N. (1969). *Fundamentals of rock mechanics*. Chapman & Hall.
Jaoul, O., Tullis, J., & Kronenberg, A. (1984). The effect of varying water contents on the creep behaviour of Heavitree quartzite. *Journal of Geophysical Research*, *89*(B6), 4298–4312. https://doi.org/10.1029/jb089ib06p04298
Jolie, E., Scott, S., Faulds, J., Chambefort, I., Axelsson, G., Gutiérrez-Negrín, L. C., et al. (2021). Geological controls on geothermal resources for power generation. *Nature Reviews Earth & Environment*, *2*(5), 324–339. https://doi.org/10.1038/s43017-021-00154-y
Kohlstedt, D. L., Evans, B., & Mackwell, S. J. (1995). Strength of the lihosphere: Constraints imposed by laboratory experiments. *Journal of Geophysical Research*, *100*(B9), 17587–17602. https://doi.org/10.1029/95jb01460
Kushnir, A. R. L., Martel, C., Champallier, R., & Wadsworth, F. B. (2017). Permeability evolution in variably glassy basaltic andesites measured under magmatic conditions. *Geophysical Research Letters*, *44*(20), 10262–10271. https://doi.org/10.1002/2017gl074042
Lamur, A., Lavallée, Y., Iddon, F. E., Hornby, A. J., Kendrick, J. E., Von Aulock, F. W., & Wadsworth, F. B. (2018). Disclosing the temperature of columnar jointing in lavas. *Nature Communications*, *9*(1), 1432. https://doi.org/10.1038/s41467-018-03842-4
Lavallée, Y., Lamur, A., Kendrick, J. E., Eggertsson, G. H., Weaver, J., Eichelberger, J. C., et al. (2020). Thermal manipulation of magma boundaries: Advancing controls on fluid flow via the Krafla Magma Testbed (KMT). In *Proceedings of 2020 World Geothermal Congress*.
Le Maitre, R. W. (1984). A proposal by the IUGS Subcommission on the Systematics of Igneous Rocks for a chemical classification of volcanic rocks based on the total alkali silica (TAS) diagram: (on behalf of the IUGS Subcommission on the Systematics of Igneous Rocks). *Australian Journal of Earth Sciences*, *31*(2), 243–255. https://doi.org/10.1080/08120098408729295
Masotta, M., Mollo, S., Nazzari, M., Tecchiato, V., Scarlato, P., Papale, P., & Bachmann, O. (2018). Crystallization and partial melting of rhyolite and felsite rocks at Krafla volcano: A comparative approach based on mineral and glass chemistry of natrual and experimental products. *Chemical Geology*, *483*, 603–618. https://doi.org/10.1016/j.chemgeo.2018.03.031
Meyer, G. G., Brantut, N., Mitchell, T. M., & Meredith, P. G. (2019). Fault reactivation and strain partitioning across the brittle-ductile transition. *Geology*, *47*(12), 1127–1130. https://doi.org/10.1130/g46516.1
Meyer, G. G., Shahin, G., Cordonnier B, B., & Violay, M. (2024). Permeability partitioning through the brittle-to-ductile transition and its implications for supercritical geothermal reservoirs. *Nature Communications*, *15*(1), 7753. https://doi.org/10.1038/s41467-024-52092-0
Mitchell, E. K., Fialko, Y., & Brown, K. M. (2015). Frictional properties of gabbro at conditions corresponding to slow slip events in subduction zones. *Geochemistry, Geophysics, Geosystems*, *16*(11), 4006–4020. https://doi.org/10.1002/2015gc006093
Mortensen, A. K., Egilson, Þ., Gautason, B., Árnadóttir, S., & Guðmundsson, Á. (2014). Stratigraphy, alteration mineralogy, permeability and temperature conditions of well IDDP-1, Krafla, NE-Iceland. *Geothermics*, *49*, 31–41. https://doi.org/10.1016/j.geothermics.2013.09.013
Murrell, S. A. F. (1965). The effect of triaxial stress systems on the strength of rocks at atmospheric temperatures. *Geophysical Journal International*, *10*(3), 231–281. https://doi.org/10.1111/j.1365-246X.1965.tb03155.x
Niu, L., Zhou, Y., Shao, T., Wang, L., Xu, X., & Rybacki, E. (2024). Experimental insights into fault reactivation and stability of carrara marble across the brittle–ductile transition. *Journal of Geophysical Research: Solid Earth*, *129*(4), e2023JB028364. https://doi.org/10.1029/2023jb028364
Olasolo, P., Juárez, M. C., Morales, M. P., Damico, S., & Liarte, I. A. (2016). Enhanced geothermal systems (EGS): A review. *Renewable and Sustainable Energy Reviews*, *56*, 133–144. https://doi.org/10.1016/j.rser.2015.11.031
Parisio, F., Lehmann, C., & Nagel, T. (2020). A model of failure and localization of basalt at temperature and pressure conditions spanning the brittle-ductile transition. *Journal of Geophysical Research: Solid Earth*, *125*(11), e2020JB020539. https://doi.org/10.1029/2020jb020539
Parisio, F., Yoshioka, K., Sakaguchi, K., Goto, R., Miura, T., Pramudyo, E., et al. (2021). A laboratory study of hydraulic fracturing at the brittle-ductile transition. *Scientific Reports*, *11*(1), 22300. https://doi.org/10.1038/s41598-021-01388-y
Passchier, C. W., & Trouw, R. A. J. (1996). *Microtectonics*. Springer.
Paterson, M. S. (1970). A high-pressure, high-temperature apparatus for rock deformation. *International Journal of Rock Mechanics and Mining Sciences & Geomechanics Abstracts*, *7*(5), 517–526. https://doi.org/10.1016/0148-9062(70)90004-5
Paulick, H., Ewen, C., Blanchard, H., & Zöller, L. (2009). The Middle-Pleistocene (~300 ka) Rodderberg maar-scoria cone volcanic complex (Bonn, Germany): Eruptive history, geochemistry, and thermoluminescence dating. *International Journal of Earth Sciences*, *98*(8), 1879–1899. https://doi.org/10.1007/s00531-008-0341-0
Reinsch, T., Dobson, P., Asanuma, H., Huenges, E., Poletto, F., & Sanjuan, B. (2017). Utilizing supercritical geothermal systems: A review of past ventures and ongoing research activities. *Geothermal Energy*, *5*(1), 16. https://doi.org/10.1186/s40517-017-0075-y
Rutter, E. (1986). On the nomenclature of mode of failure transitions in rocks. *Tectonophysics*, *122*(3–4), 381–387. https://doi.org/10.1016/0040-1951(86)90153-8
Rutter, E. H., & Brodie, K. H. (2004). Experimental intracrystalline plastic flow in hot-pressed synthetic quartzite prepared from Brazilian quartz crystals. *Journal of Structural Geology*, *26*(2), 259–270. https://doi.org/10.1016/s0191-8141(03)00096-8
Rybacki, E., Gottschalk, M., Wirth, R., & Dresen, G. (2006). Influence of water fugacity and activation volume on the flow properties of fine-grained anorthite aggregates. *Journal of Geophysical Research*, *111*(B3), B03203. https://doi.org/10.1029/2005JB003663
Rybacki, E., Niu, L., & Evans, B. (2021). Semi-Brittle deformation of carrara marble: Hardening and twinning induced plasticity. *Journal of Geophysical Research: Solid Earth*, *126*(12), e2021JB022573. https://doi.org/10.1029/2021jb022573
Rybacki, E., Reinicke, A., Meier, T., Makasi, M., & Dresen, G. (2015). What controls the mechanical properties of shale rocks? – Part I: Strength and Young's modulus. *Journal of Petroleum Science and Engineering*, *135*, 702–722. https://doi.org/10.1016/j.petrol.2015.10.028
Rybacki, E., Schuster, V., Starke, J., & Incel, S. (2026). Mechanical data for: High temperature friction and strength of felsite and basalt: Implications for supercritical EGS at Krafla, Iceland [Dataset]. *Mendeley Data, V1*. https://doi.org/10.17632/w29g66ky9k.1
Scholz, C. (2019). *The mechanics of earthquakes and faulting*. Cambridge Univerty Press.
Schuler, J., Greenfield, T., White, R. S., Roecker, S. W., Brandsdóttir, B., Stock, J. M., et al. (2015). Seismic imaging of the shallow crust beneath the Krafla central volcano, NE Iceland. *Journal of Geophysical Research: Solid Earth*, *120*(10), 7156–7173. https://doi.org/10.1002/2015jb012350
Sheorey, P. R. (1997). *Empirical rock failure criteria*. A.A. Balkema.
Siratovich, P. A., Villeneuve, M. C., Cole, J. W., Kennedy, B. M., & Bégué, F. (2015). Saturated heating and quenching of three crustal rocks and implications for thermal stimulation of permeability in geothermal reservoirs. *International Journal of Rock Mechanics and Mining Sciences*, *80*, 265–280. https://doi.org/10.1016/j.ijrmms.2015.09.023
Stesky, R., Brace, W., Riley, D., & Robin, P.-Y. (1974). Friction in faulted rock at high temperature and pressure. *Tectonophysics*, *23*(1–2), 177–203. https://doi.org/10.1016/0040-1951(74)90119-x
Stesky, R. M. (1978). Rock friction-effect of confining pressure, temperature, and pore pressure. *Pure and Applied Geophysics*, *116*(4–5), 690–704. https://doi.org/10.1007/bf00876532
Stimac, J., Goff, F., & Goff, C. J. (2015). Chapter 46 - Intrusion-Related geothermal systems. In H. Sigurdsson (Ed.), *The encyclopedia of volcanoes* (2nd ed., pp. 799–822). Academic Press.

Tembe, S., Lockner, D. A., & Wong, T.-F. (2010). Effect of clay content and mineralogy on frictional sliding behavior of simulated gouges: Binary and ternary mixtures of quartz, illite, and montmorillonite. *Journal of Geophysical Research*, *115*(B3), B03416. https://doi.org/10.1029/2009jb006383

Violay, M., Gibert, B., Mainprice, D., Evans, B., Dautria, J.-M., Azais, P., & Pezard, P. (2012). An experimental study of the brittle-ductile transition of basalt at oceanic crust pressure and temperature conditions. *Journal of Geophysical Research*, *117*(B3), B03213. https://doi.org/10.1029/2011jb008884

Violay, M., Heap, M. J., Acosta, M., & Madonna, C. (2017). Porosity evolution at the brittle-ductile transition in the continental crust: Implications for deep hydro-geothermal circulation. *Scientific Reports*, *7*(1), 7705. https://doi.org/10.1038/s41598-017-08108-5

Violay, M., Passelegue, F., Spagnuolo, E., Di Toro, G., & Cornelio, C. (2019). Effect of water and rock composition on re-strengthening of cohesive faults during the deceleration phase of seismic slip pulses. *Earth and Planetary Science Letters*, *522*, 55–64. https://doi.org/10.1016/j.epsl.2019.06.027

Watanabe, N., Egawa, M., Sakaguchi, K., Ishibashi, T., & Tsuchiya, N. (2017). Hydraulic fracturing and permeability enhancement in granite from subcritical/brittle to supercritical/ductile conditions. *Geophysical Research Letters*, *44*(11), 5468–5475. https://doi.org/10.1002/2017gl073898

Watanabe, N., Numakura, T., Sakaguchi, K., Saishu, H., Okamoto, A., Ingebritsen, S. E., & Tsuchiya, N. (2017). Potentially exploitable supercritical geothermal resources in the ductile crust. *Nature Geoscience*, *10*(2), 140–144. https://doi.org/10.1038/ngeo2879

Watanabe, N., Saito, K., Okamoto, A., Nakamura, K., Ishibashi, T., Saishu, H., et al. (2020). Stabilizing and enhancing permeability for sustainable and profitable energy extraction from superhot geothermal environments. *Applied Energy*, *260*, 114306. https://doi.org/10.1016/j.apenergy.2019.114306

Yapparova, A., Lamy-Chappuis, B., Scott, S. W., Gunnarsson, G., & Driesner, T. (2023). Cold water injection near the magmatic heat source can enhance production from high-enthalpy geothermal fields. *Geothermics*, *112*, 102744. https://doi.org/10.1016/j.geothermics.2023.102744

Zang, A., Oye, V., Jousset, P., Deichmann, N., Gritto, R., McGarr, A., et al. (2014). Analysis of induced seismicity in geothermal reservoirs – An overview. *Geothermics*, *52*, 6–21. https://doi.org/10.1016/j.geothermics.2014.06.005

Zhang, L., He, C., Liu, Y., & Lin, J. (2017). Frictional properties of the south China sea oceanic basalt and implications for strength of the manila subduction seismogenic zone. *Marine Geology*, *394*, 16–29. https://doi.org/10.1016/j.margeo.2017.05.006

Zierenberg, R. A., Schiffman, P., Barfod, G. H., Lesher, C. E., Marks, N. E., Lowenstern, J. B., et al. (2013). Composition and origin of rhyolite melt intersected by drilling in the Krafla geothermal field, Iceland. *Contributions to Mineralogy and Petrology*, *165*(2), 327–347. https://doi.org/10.1007/s00410-012-0811-z

Zoback, M. D. (2007). *Reservoir geomechanics*. Cambridge University Press.